

Carbon Fiber Composite **Pyramidal Lattice Structures**

A Thesis
Presented to
the faculty of the School of Engineering and Applied Science
University of Virginia

In Partial Fulfillment
Of the requirements for the Degree
Master of Engineering (Engineering Physics)

By
Kevin A. Finnegan
May 2007

Approval Sheet

This thesis is submitted in partial fulfillment of the requirements for the degree of

Master of Engineering
(Engineering Physics)

Kevin A. Finnegan, Author

This thesis has been read and approved by the examining committee:

Haydn N. G. Wadley, Advisor

Sean Agnew, Committee Chair

Stuart Wolf

Vikram Deshpande

Mark Aronson

Accepted for the School of Engineering and Applied Science:

Dean, School of Engineering
Applied Science
May, 2007

Abstract

Cellular lattice truss structures made from light metals with interconnected porosity have recently gained attention as an emerging materials technology for ultra lightweight structural design. They appear of particular interest for use as the cores of sandwich panels loaded in bending. Several cell topologies with pyramidal, tetrahedral and 3D Kagome unit cell structures have been proposed. Due to their open and highly periodic cell topology, they all provide high strength and reasonable stiffness while also permitting their open void spaces to be used for other purposes such as cross flow heat exchange. The pyramidal lattice structures investigated to date have been fabricated from metal alloys by investment casting, sheet metal forming or by rod assembly followed by metallic bonding using brazing or laser welding. The specific strength of these lattices has been increased by the use of the sheet forming approach which permits lattice fabrication from high specific strength aluminum and titanium alloys. Carbon fiber reinforced polymer (CFRP) composites have an even higher specific strength than the light alloys and have been utilized as facesheet materials in sandwich panels for demanding high strength applications. However due fabrication challenges, CFRP composites have not been widely used for the cellular core. Here, novel methods for creating pyramidal lattice core sandwich panels from CFRP composites have been investigated and the most promising used to manufacture and evaluate the through thickness compressive strength of CFRP composite lattice core sandwich panel structures. In the most preferred approach, both the facesheets and the core were created from pre-cured, bi-axial carbon fiber laminated plates. The cores were cut from the laminates using a waterjet cutting method in such a manner that 50% of the

fiber tows were in the truss loading direction. These core components were snap fitted and adhesively bonded to form pyramidal cores that were then epoxy bonded to facesheets. Sandwich panels with relative densities ranging from 1-10% were constructed and tested in compression. The strength of the structures ranged from 1-10 MPa, increasing with relative density. The mechanisms of core failure were identified by a combination of in-situ photography during testing and careful metallographic assessments of failed specimens. These observations were then used to develop a micromechanical model for predicting the strength of these structures from theories for the strength and modulus of unidirectional fibrous composites. It adequately predicted the observed behavior of the panels and identified the important roles of fiber kinking and interplay delamination in determining the maximum strength of these structures. These composite lattices have the highest specific strength of any cellular structure reported to date.

Table of Contents

List of Figures.....	iii
List of Tables.....	v
List of Symbols.....	vi
Chapter	
1. Introduction.....	1
1.1 Background.....	1
1.1.2 Core Strength Considerations.....	9
1.1.3 Manufacturing and Modeling Considerations.....	12
1.2 Goals of the Thesis.....	13
1.2.1 Thesis Outline.....	14
2. Pultruded Fabrication Approach.....	15
2.1 Manufacturing Method.....	15
2.2 Results.....	18
2.3 Discussion.....	20
3. Unidirectional Laminate Fabrication Approach.....	23
3.1 Manufacturing Method.....	23
3.2 Results.....	25
3.3 Discussion.....	27
4. Bi-axial Laminate Fabrication Approach.....	29
5. Mechanical Testing Methodology.....	35
5.1 Pyramidal Lattice Compression Tests.....	35
5.2 Laminate Compression Tests.....	37
5.2.1 Combined Clamped/End Loading Tests.....	37
5.2.2 Unclamped Compression Tests.....	38
6. Results.....	39
6.1 Laminate Properties.....	39
6.2 Pyramidal Core Compression Results.....	42

7. Micromechanical Modeling	45
7.1 Elastic Properties.....	46
7.2 Collapse Strength.....	48
7.2.1 Plastic Microbuckling of the Composite Struts.....	48
7.2.2 Delamination Failure of the Struts.....	50
7.2.3 Euler Buckling of the Struts.....	50
7.3 Comparisons and Discussion.....	51
8. Discussion	57
9. Conclusions	60
References	62
Appendix A	66
Appendix B	67

List of Figures

Figure 1.1	Natural Cellular Materials	3
Figure 1.2	Strength vs. Density Material Selection Charts	4
Figure 1.3	Cellular Metal Products	5
Figure 1.4	2-Dimensional Cellular Solids	6
Figure 1.5	Hornbill Beak	7
Figure 1.6	Metal Lattice Truss Structures	8
Figure 1.7	Failure Mechanisms for Fibrous Composites	13
Figure 2.1	Pyramidal Core Fabrication Process	16
Figure 2.2	Single Cell Pyramidal Truss core	17
Figure 2.3	Pultruded Rod Core Stress-Strain Response	19
Figure 2.4	Strength Coefficient vs. Relative Density	19
Figure 2.5	Failure Mechanisms in Pultruded Rod core	20
Figure 2.6	Truss/Faceplate junction	21
Figure 3.1	Unidirectional Laminate Cutout Pattern	23
Figure 3.2	Unidirectional Assembly Process	24
Figure 3.3	Unidirectional Laminate Core Geometry	25
Figure 3.4	Stress-Strain Response for Unidirectional Cores	26
Figure 3.5	Strength Coefficient vs. Relative Density	27
Figure 3.6	Failure Mechanisms for Unidirectional Core	27
Figure 4.1	Bi-axial Laminate Manufacturing and Assembly	30
Figure 4.2	Core Geometry and Variables	31
Figure 4.3	Two Node Designs	32
Figure 4.4	Completed Bi-axial Sandwich Panel	33

Figure 5.1	Pyramidal Compression Test Setup	36
Figure 5.2	Combined Loading Test Rig	38
Figure 6.1	Laminate Stress Strain Results	40
Figure 6.2	Clamped Test Failure Zones	41
Figure 6.3	Unclamped Test Failures	42
Figure 6.4	Pyramidal Core Stress-Strain Response	43
Figure 6.5	Modulus and Strength vs. Relative density	43
Figure 6.6	Near-Node Failure	44
Figure 6.7	Euler Buckling Failure	44
Figure 7.1	Cutout Pattern and Fiber Misalignment	45
Figure 7.2	Truss Deflection	47
Figure 7.3	Predicted Modulus vs. Relative Density	52
Figure 7.4	Predicted Strength vs. Relative Density	53
Figure 7.5	Strength Coefficient vs. Relative Density	55
Figure 8.1	Strength vs. Density for Various Pyramidal Panels	58

List of Tables

Table 2.1	CFRP sandwich panel component properties	16
Table 2.2	Fiberglast 2000/2006 Epoxy Properties	17
Table 3.1	Unidirectional Laminate Properties	23
Table 3.2	Hysol EP-120 Epoxy Properties	24
Table 4.1	Core Design Parameters	31
Table 4.2	List of truss lengths and relative densities	32
Table 4.3	Laminate Architecture and Properties	33
Table 5.1	Compression Test Strain Rates	36
Table 6.1	Summary of Laminate Compression Tests	39

List of Symbols

$\bar{\rho}$	Relative Density.....	dimensionless
ρ_*	Density of Cellular Material.....	g/cm^3
ρ_s	Density of Solid Material.....	g/cm^3
σ_f	Foam Peak Strength.....	MPa
σ_s	Solid Peak Strength.....	MPa
$k_{1,2,3}$	Foam Geometry Coefficients.....	dimensionless
E_s	Solid Elastic Modulus.....	MPa
E_f	Foam Elastic Modulus.....	MPa
σ_l	Lattice Peak Strength.....	MPa
E_l	Lattice Elastic Modulus.....	MPa
v_f	Fiber Volume Fraction.....	dimensionless
l	Truss Length.....	mm
w_{node}	Node Width.....	mm
d	Rod Truss Diameter.....	mm
ω	Truss Inclination Angle.....	degrees
Σ	Strength Coefficient.....	dimensionless
σ_p	Pyramidal Core Peak Compressive Strength.....	MPa
σ_{max}	Peak Compressive Strength of Solid Truss Material.....	MPa
$\bar{\Sigma}$	Average Structural Efficiency.....	dimensionless
F_a	Axial Force.....	N
F_n	Node Shear Force.....	N
F	Total Compressive Force.....	N
t_{face}	Facesheet Thickness.....	mm
τ_a	Adhesive Shear Strength.....	MPa
h_{tab}	Truss Tab Height.....	mm

l_{tab}	Truss Tab Length.....	mm
h_{core}	Core Height.....	mm
t	Truss Thickness.....	mm
w	Truss Width.....	mm
h	Node Height.....	mm
b	Outer Node Length.....	mm
c	Inner Node Length.....	mm
$e_{1,2}$	Local Fiber Cartesian Coordinates.....	unit vectors
σ_c	Compressive Plastic Microbuckling Strength.....	MPa
τ_y	Matrix Longitudinal Shear Strength.....	MPa
E_p	Pyramidal Core Elastic Modulus.....	MPa
ϕ	Fiber Misalignment Angle.....	degrees
δ	Vertical Displacement.....	mm
F_S	Shear Force.....	N
I	Second Moment of Inertia.....	mm ⁴
σ	Applied Through-Thickness Nominal Stress.....	MPa
ε	Applied Through-Thickness Nominal Strain.....	dimensionless
\bar{l}	Geometric Core Parameter.....	dimensionless
\bar{b}	Geometric Node Parameter.....	dimensionless
β	Kink Band Angle.....	degrees
τ^∞	In-plane Shear.....	MPa
σ_{dl}	Delamination Failure Stress.....	MPa
P_E	Euler Buckling Load.....	N
\bar{E}_s	Material Strength Parameter.....	dimensionless

Chapter 1

Introduction

High performance, minimum weight structures for aerospace applications frequently exploit sandwich panel construction concepts. These sandwich panels utilize strong, stiff, light materials for their faces and foams, corrugations and honeycombs for their cores. Each core topology has strengths and weaknesses. Honeycomb cores combine the best stiffness and shear strength. However, their closed cellular structure renders them vulnerable to internal corrosion and delamination which can be difficult to inspect and repair. Lattice truss core structures have begun to be investigated as possible candidates for open cell sandwich panels. Some appear competitive with honeycombs in both stiffness and strength. Their open cell structure creates novel possibilities for multifunctional uses. These truss structures are currently made from light metals by sheet forming or casting processes. This thesis explores novel methods for making truss structures from fiber reinforced polymer composites with the goal of improving the specific strength of ultralight sandwich panel structures.

1.1 Background

The emergence of light, stiff, strong materials such as aluminum and titanium alloys in the last century, and more recently carbon fiber composites, has facilitated the design of many lightweight aerospace structures [1]. Beginning with the advent of corrugated cardboard in the 1870's, sandwich panel structures have been developed in parallel as a weight efficient concept for supporting bending loads [2]. In this approach two thin face sheets of a high specific strength material are separated by a thick core, usually made of light, but lower strength materials such as Nomex (a paper honeycomb), polymer foams, balsa wood, or other cellular materials [1]. The core supports the faces maintaining them far from the panel's neutral axis where the tensile and compressive membrane stresses are a maximum [3]. The core can also serve many other roles; (i) if it resists crushing, it enables plate action to be maintained even in high intensity loading situations [1], (ii) it can stabilize the compressively deforming panel face against

wrinkling during plate bending [4] and (iii) it can sometimes provide additional functionalities such as thermal insulation [5] or cross-flow heat exchange [6, 7]. Many of today's highest specific stiffness and strength structures combine light, high strength materials with these sandwich panel construction concepts [8, 9].

In bulk materials, voids and pores are generally considered undesirable imperfections since they decrease the stiffness and strength [10]. Observations of natural materials however, indicate cellular materials with appropriately structured voids and pores, like bone or wood, can be efficiently utilized for load support [12]. These constructs are particularly advantageous when configured as cellular solids surrounded by thin, dense (strong) layers [53]. They often serve multifunctional purposes as well. Bones for instance have structures with a hard outer layer used to carry stresses and a lightweight interior that houses other tissue while maintaining a high bending resistance [54].

The architectures of these natural cellular materials fall into one of two categories [10, 11]. Those consisting of networked ligaments connected at nodes are termed *open cell* structures. Those which have membrane walls entirely surrounding the voids are *closed cell* structures. Figure 1.1 shows several examples of natural materials from each of these categories. Studies of their morphology has led to the field of *cellular solids* [12]. Cellular solids lie at the interface between materials (whose properties are sample size independent) and structures.

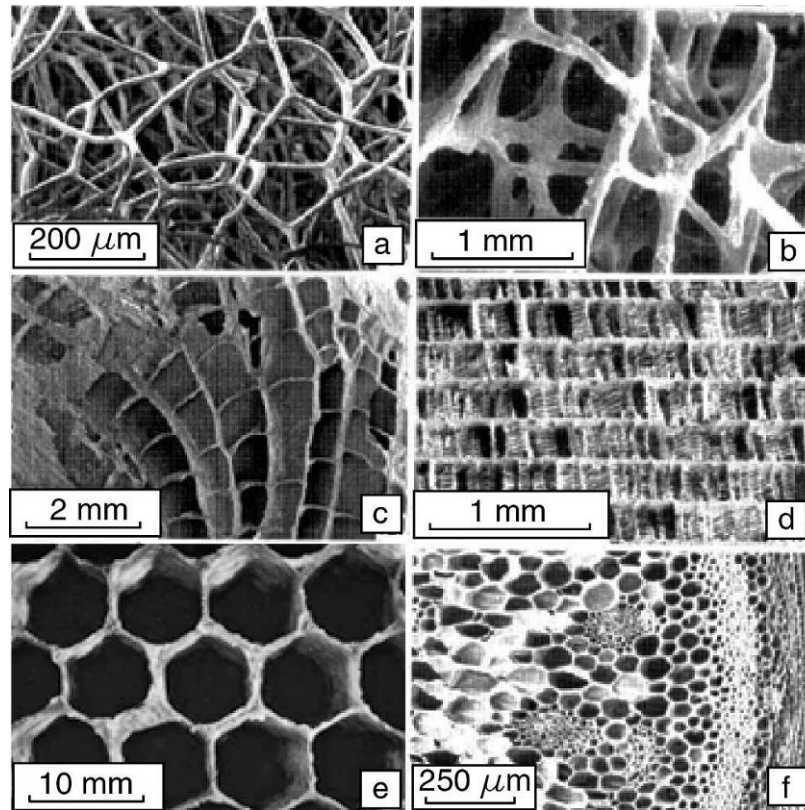


Fig. 1.1 Natural cellular materials. a) Sponge b) cancellous bone c) coral d) cuttlefish bone e) Bee honeycomb f) plant stalk. Note that the top two structures are open cell, whereas the others are closed in at least two directions. [12]

It is interesting to use graphical methods suggested by M. F. Ashby and his collaborators [13,14] to compare the properties of cellular materials with other engineering materials. The Ashby charts [15] shown in Figure 1.2, enable comparisons of the strength and stiffness ranges of available materials to be plotted against their density. It can be seen that the lowest density materials are all cellular in nature. Most have pore sizes on the order of a few millimeters down to the nano-scale [16]. The lightest strongest/stiffest materials that are most desirable for ultra-light structures lie to the upper left of these diagrams.

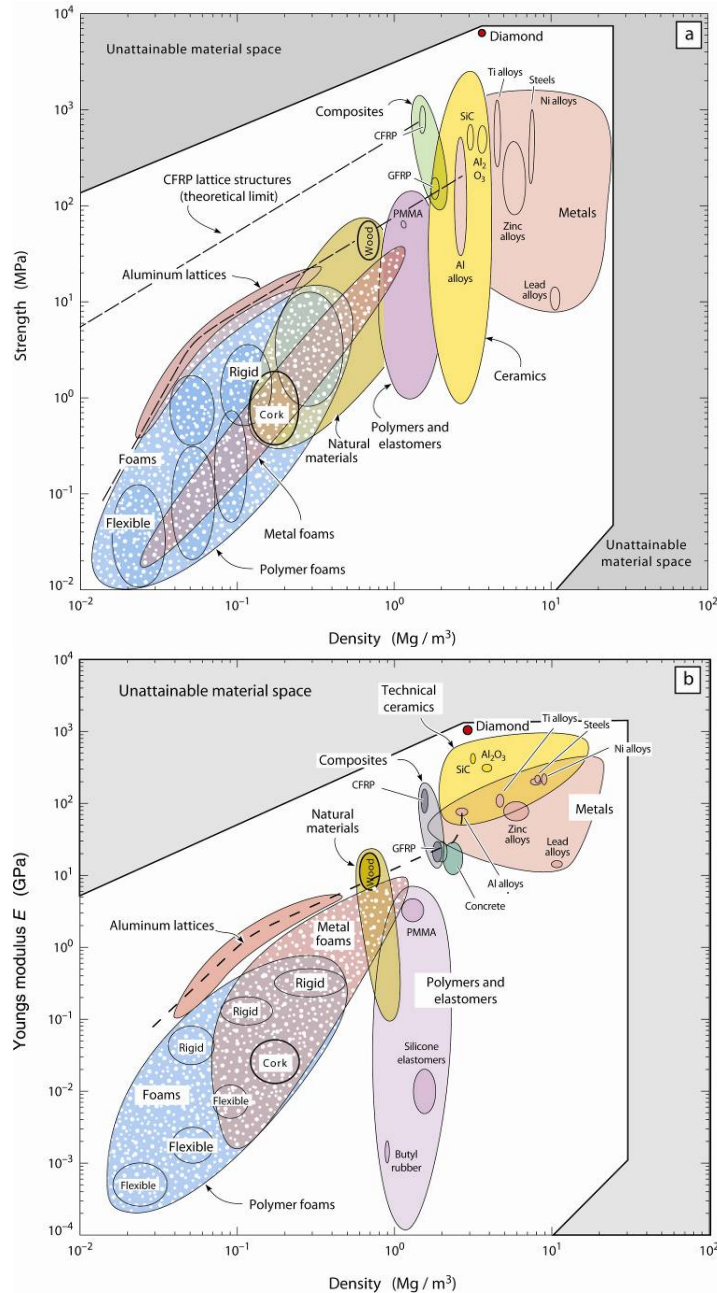


Fig. 1.2 (a) Strength vs. Density and (b) Modulus vs. Density charts for engineering materials. In both charts there is a gap in the low density – high strength/stiffness region which could be filled by cellular forms of composites or ceramics. The predicted behavior for aluminum lattices is shown as a dashed line in both charts. The CFRP dashed line refers to the upper bound strength of a composite lattice.

The increasing demand for light weight sandwich panel designs, (surfboards, skis, bridges etc.) has stimulated intense interest in synthetic cellular solids made from polymers [5], metals [17] and even ceramics [18]. Initial work focused upon polymers to

which foaming agents were added in the liquid state [5]. The demand for higher strength core materials led to the emergence of strong (but brittle) polymer foams [5,19,20]. Significant growth in the manufacturing of engineered foams has taken place since the 1970's [10]. The continued interest in higher strength (and stiffness) foams led to numerous methods for making metal foams from castable alloys with varying cell size and morphologies [10]. Examples of several commercial metal foams are shown in Figure 1.3. New methods for creating foams from polymers and ceramics have expanded the property ranges of cellular solids. Polymers in particular have can be made into flexible or stiff foams depending on the properties of the parent material from which they are made [16].

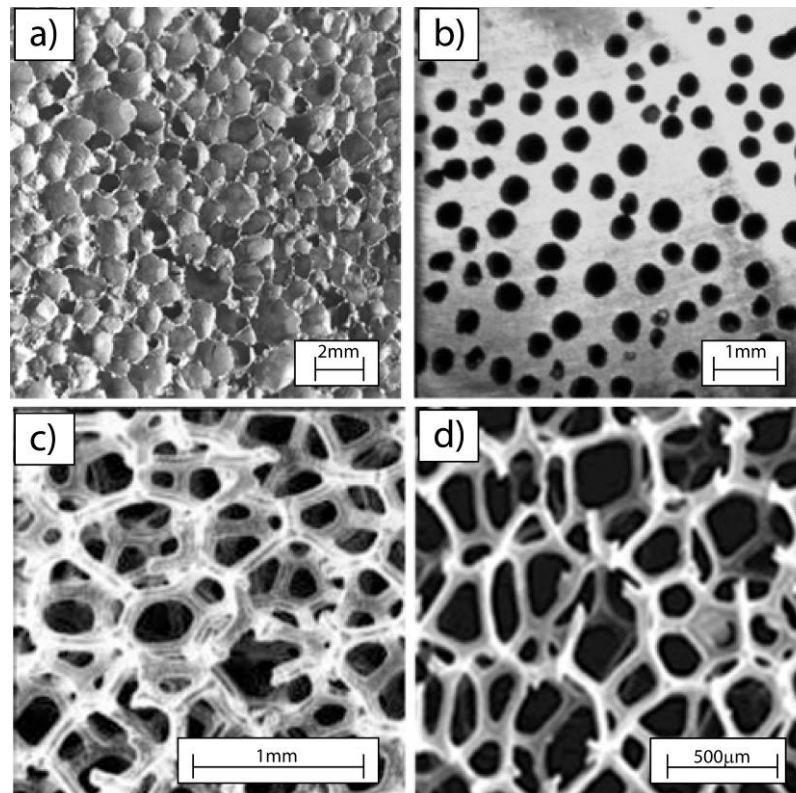


Fig. 1.3 Cellular metal products. a) closed cell (ALPORAS) Al foam. b) closed cell (Lotus-type) GASAR processed 304 stainless steel containing unidirectional pores. c) open cell (Duocel) Al foam and d) open cell (Incofoam) Ni foam [21]

While foams were the first venture in creating synthetic cellular solids, their stochastic topology is not structurally optimized for load support. Within cellular solids there is a subclass of materials which exhibit a high degree of order in their structures. Prismatic constructions have 2-dimensional periodicity which increases the shear strength of a material in the web direction. The plant stalk and in Figure 1.1 is an example of a prismatic cellular solid found in nature. Honeycombs can be created by rotating the corrugated core so that the webs are connected to the facesheets. Honeycombs are perhaps the most successful example of cellular structures to date as they are highly efficient at supporting loads applied along their webs [12]. Hexagonal honeycombs, such as Nomex [22], are commonly used as core material in lightweight sandwich panels where the face sheets then seal the two open faces of each cell. Several of these periodic cellular topologies are shown in Figure 1.4. In the prismatic case, the cell topology inhibits cell to cell transport in two directions while honeycomb cells are fully closed.

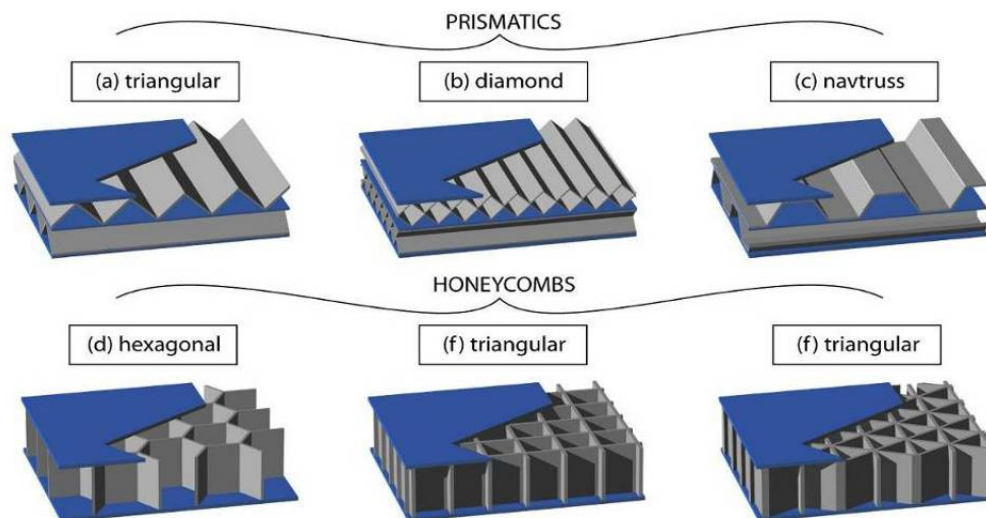


Fig. 1.4 2-Dimensional cellular solids arranged as prismatic and honeycomb style sandwich panel cores.

Lattice truss structures represent a third emerging subclass of cellular. Bird bones like the beak shown in Figure 1.5 are naturally optimized to support compressive loads by means of a thin outer shell which is impeded from buckling via bone trusses [55]. This is achieved while remaining as weight efficient as possible. A similar concept has been exploited for sandwich panels with lattice truss cores as shown in Figure 1.6. The improvement in strength to weight ratio is based on the principle that truss members primarily experience axial tension or compression when the panels are loaded in shear or bending. It will be shown later that these stretch dominated structures are capable of withstanding higher loads than their bending dominated foam counterparts [9].

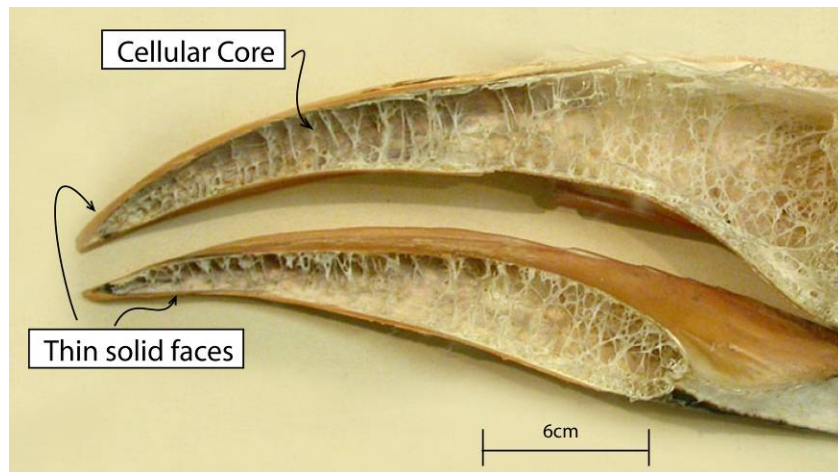


Fig. 1.5 Cross section of a Hornbill bird beak. Lightweight bone struts fill the space between the thin beak-shell; very similar to lattice truss sandwich panels [55].

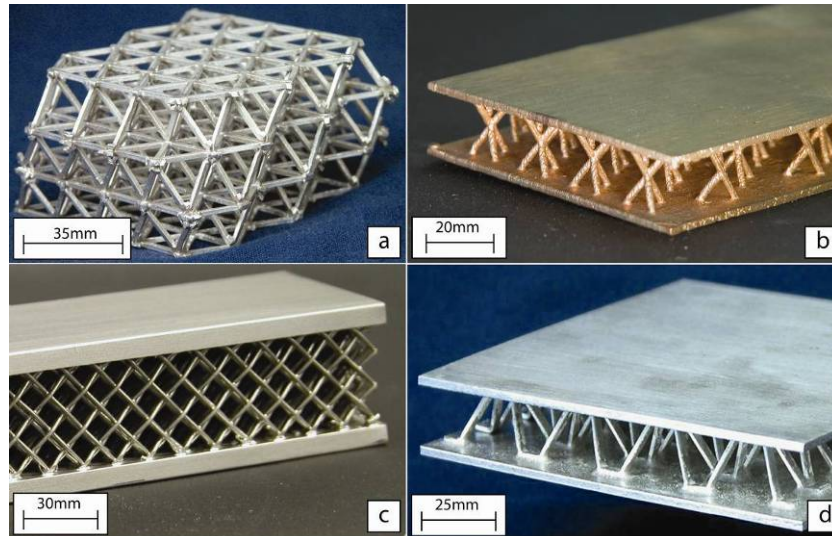


Fig. 1.6 Metal lattice truss structures with various relative density ($\bar{\rho}$) cores. a) sheet folded aluminum tetrahedral lattice block $\bar{\rho}=5\%$ b) cast Cu-1.8%Be alloy kagome sandwich panel $\bar{\rho}=2\%$ c) Woven 304SS textile sandwich panel $\bar{\rho}=12\%$ d) expanded aluminum sheet pyramidal lattice panel $\bar{\rho}=2\%$

The ideal sandwich panel core is both light and strong meeting the aim of maintaining face sheet separation during localized through thickness compression (indentation) and bending [4]. Strong cores are especially necessary in intensely loaded situations such as those encountered in impacts. The core topology affects both the modulus and strength of a core structure [23]. Hexagonal honeycomb, corrugated and stochastic foam core topologies have all been used with the ultimate selection dictated by the structural loads and other desired functionalities such as sound absorption [22], cross flow heat exchange [6, 7] or thermal insulation [12, 24]. Periodic lattice truss structures have also begun to be investigated as potential high performance core topologies with useful multifunctional attributes [8]. Some, made from light metallic alloys, have been shown to be as efficient as honeycombs while also offering better cross flow heat exchange options [6] and significant impact load mitigation [25].

As the discussion above has indicated, there are many cellular material core options available. The Ashby chart in Figure 1.2, enables an assessment of the numerous

choices [15]. The preferred core material resides to the upper left of this chart and brittle polymer foams and honeycombs have been a good choice for many applications. Recent data for aluminum lattice structures [26] has been added to the chart in Figure 1.2 and it is apparent that these structures (and honeycombs counterparts, if they could be made from the same high strength alloys) are the most preferable, especially when the use temperature exceeds the allowable limits of polymeric cores. The chart also identifies the regions of unattainable material properties as described by Ashby et al [27]. It can be seen that a significant gap (or hole) exists between today's light weight materials and the upper theoretical bounds. The development of a core structure that might fill this hole is the focus of this thesis.

1.1.2 Core strength considerations

The leftward and downward extension of material properties in Figure 1.2 has been achieved by creating cellular counterparts of engineering polymers and metals. For each material, the cell topology establishes the strength - relative density relation, $\bar{\rho}$, defined here as the density of the cellular material divided by the density of the solid from which it is made (ρ_*/ρ_s). The Voight upper bound for the properties of a porous material falls in a linear manner as the pore fraction increases [27]. A key goal of cellular materials research is to create cell topologies that approach this limit.

Several studies have explored the properties of foams and lattice materials [9,12,19,23,28]. Foams can be classified as bending-dominated structures. The failure modes on the cellular level are due to membrane or ligament bending or buckling [9,23].

Analysis of the bending mode of failure gives a failure strength, σ_f , versus relative density relationship of the form:

$$\sigma_f = k_1 \sigma_s \bar{\rho}^{\frac{3}{2}} \quad (1.1a)$$

Where σ_s is the strength of the parent solid material and k_1 a cell topology dependent, geometric coefficient that measures the load supporting efficiency. If the struts are slender, failure occurs by buckling and the strength depends on the solid's elastic modulus, E_s , and the foam's relative density;

$$\sigma_f = k_2 E_s \bar{\rho}^2 \quad (1.1b)$$

Where k_2 is another topology dependent coefficient. In both cases, the elastic modulus of the foam, E_f , depends upon the square of the relative density:

$$E_f = k_3 E_s \bar{\rho}^2 \quad (1.1c)$$

Where k_3 is a topology coefficient. These relations predict well the data shown in Figure 1.2 for foams and most natural cellular materials. The power law dependence is far from the upper limit of a linear dependence upon $\bar{\rho}$ [23].

Lattice topology structures have been developed to promote truss deformation of core members in a stretch dominated manner. That is, due to their topology, the constituent truss members of a sandwich panel structure experience some bending moments but undergo primarily axial compression or tension when the panel is subjected to bending. The failure of these materials is stretch dominated. Deshpande and Fleck [9,56] have analyzed the micromechanical response of lattice structures and have shown that if the trusses fail by plasticity, the predicted strength of lattice structures, σ_l , depends linearly upon relative density:

$$\sigma_l \propto \sigma_s \bar{\rho} \quad (1.2a)$$

Where σ_s , is the yield strength of the solid material. In this case, the elastic modulus, E_l , of the lattice is given by:

$$E_l \propto E_s \bar{\rho} \quad (1.2b)$$

Both their strength and elastic modulus have been predicted to fall linearly with relative density (with a slope of 1 in Figure 1.2a) when the trusses collapse by plastic deformation [23,28]. As the relative density decreases, these structures can far out perform their stochastic counterparts. However, when the relative density becomes very low, lattices with now very slender trusses buckle in compression and their strength then falls off with $\bar{\rho}$, with a slope of 3 in Figure 1.2a because this mechanism is analogous to that modeled in equations (1.1b,c).

Equations (1.1 and 1.2) highlight the power-law dependence of material properties on relative density. The power law exponent is dictated by the operative failure modes. Bending or buckling modes which dominate foam failure cause their strength to fall with a slope of 1.5-2 in Figure 1.2a. Foams are also not geometrically arranged to optimally pick up the applied stresses, and it can be seen in Figure 1.2a that the two effects combine, resulting in strength reductions of factors of ten or so compared to lattices made from the same material [23].

The discussion above indicates that the compressive strength of cellular materials is governed by just three factors; the cell topology, the relative cell density and the specific strength of the material used to make the cellular structure. Carbon fiber reinforced polymer (CFRP) composites have very high specific strengths and stiffnesses when loaded in tension in the fiber direction [29]. If lattices could be fabricated from

such materials, and their strength fell linearly with decreasing relative density, they would fall into the region in Figure 1.2. They might then fill a hole in material property space [27].

1.1.3 Manufacturing and modeling considerations

Methods for creating metallic lattice structures have generally focused on casting [30] or plastic deformation of perforated metal sheets [31]. None of these approaches appear suitable for creating lattice truss materials from brittle, high strength materials like polymeric composites. Methods for developing high quality CFRP composite lattice core sandwich panels must be investigated in order to experimentally evaluate the benefit of such materials over current high-strength metal sandwich panel products. Fibrous composites also fail differently to metals. New models for predicting the strength of composite lattice structures that incorporate their relevant failure modes need to be developed in order to design structures with the best lightweight performance.

The most common failure modes for fibrous composites under compression are shown in Figure 1.7. For loads applied to the reinforcement fiber ends directly, matrix splitting is induced followed by fiber brooming. Matrix splitting is a weak failure mode as the peak strength is determined by the matrix alone, but simple constraints at the load ends of a fibrous composite, via caps or clamps, will prevent brooming from occurring and activate one of the stronger (more desirable) failure mechanisms [29]. The familiar Euler buckling mode occurs for sufficiently slender composite beams whereas elastic microbuckling is dictated by the composite shear and axial elastic moduli and not the geometry of the column [32]. For the majority of engineered fibrous composites arranged in a laminated structure, inter-ply delamination and plastic microbuckling are the

operative failure modes under compression [29]. The strength of a CFRP lattice structure is likely to be controlled by one of these mechanisms of failure and it is a goal of this dissertation to identify the operative failure modes and explore the possibility of avoiding low strength mechanisms of truss failure.

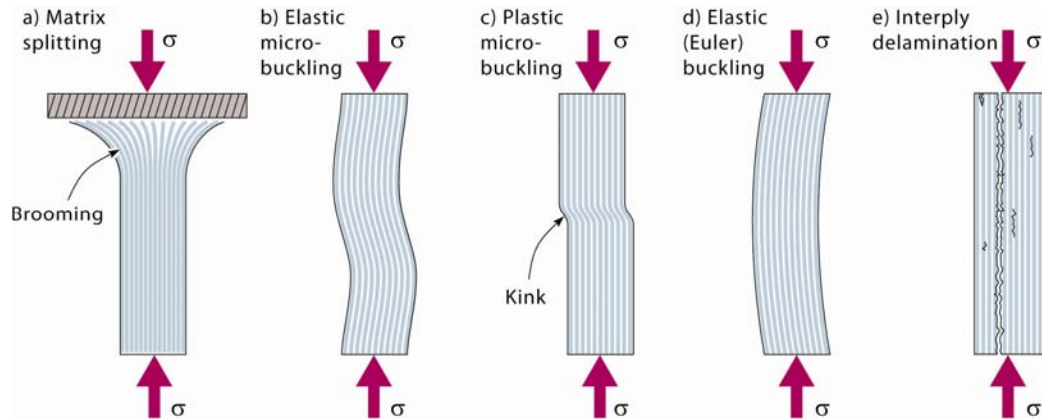


Fig. 1.7) Failure mechanisms for unidirectional fiber reinforced composites loaded in axial compression.

1.2 Goals of the thesis

This thesis explores the fabrication and mechanical behavior of a pyramidal lattice structure made from CFRP composites. It will be shown that a CFRP composite lattice core, if properly constructed, can lead to new lightweight, high strength structures. Interestingly, it will also be shown that while these structures have enhanced levels of specific strength, they do not fill the gap in specific stiffness identified in Figure 1.2b. Several methods for constructing CFRP composite lattice core sandwich panels have been identified and their deficiencies investigated. Many of these originate at the nodal connections between trusses and facesheets and the thesis experimentally explores several concepts for reducing node failure. The best of these methods is used to fabricate test structures that permit an examination of the relationship between the lattice strength

and the relative density of the core. The truss failure modes have been identified and used to propose new micromechanics-based relationships between lattice strength and relative density for fiber reinforced composite systems.

1.2.1 Thesis Outline

The layout of the thesis is as follows: Chapters 2,3 and 4 detail the various, different approaches investigated for fabrication of the lattice truss structures. Chapter 5 describes the mechanical testing procedures used to experimentally determine the material response both of the best lattice concept and constituent materials. Chapter 6 reports the mechanical property measurements and failure mode analysis. Chapter 7 develops a micromechanical analysis of panel properties based on the observed failure modes of the lattice. Chapter 8 discusses the significance of the work. The dissertations principle observations are summarized in a conclusions Chapter 9.

Chapter 2 Pultruded Rod Fabrication Approach

2.1 Manufacturing method

Many methods for making polymeric and metallic cellular structures have been developed [31,33-37]. These methods of fabrication are reliant on liquid state foaming [10], investment casting, sheet patterning and bending of ductile polymer or metal sheet [31] and most recently, extrusion [38]. However none appear feasible for fabricating pyramidal lattices from brittle fiber reinforced composites. One group has fabricated a pyramidal cellular structure by the hand lay-up of pre-impregnated tapes through use of complicated mandrels which are disassembled and removed from the core after curing [35]. A second group has fabricated lattices by inserting pre-cured pin trusses through both faces of a composite face sandwich panel with low density polymer core [36]. This pin based approach produces a lightweight truss core, but the insertion process results in weak truss-facesheet nodes.

Fibrous composites are highly anisotropic. Their best material properties occur when loads are applied along the fiber axis. The first approach investigated for lattice fabrication has utilized pultruded rods which provide a highly oriented unidirectional composite column that is relatively inexpensive to fabricate. The unidirectional pultruded rod approach to sandwich panel fabrication is shown in Figure 2.1. The rods were pultruded by Graphitstore.com (Buffalo Grove, IL) using 220 GPa modulus carbon fiber in a vinylester matrix with a fiber volume fraction, v_f , of 62%. Table 2.1 lists the rod properties. To make sandwich panels, 0/90° laminated facesheets 1.5mm thick (also from Graphitstore) were first drilled to create a clover leaf hole pattern with each hole oriented at a 45° angle with respect to the facesheet shown in Figure 2.2a. Faceplate

laminates properties are given in Table 2.1. The 2mm diameter pultruded carbon fiber rods were then inserted through the holes in the faceplates and adhesively bonded in place using Fiberglass 2000/2060 epoxy [39]. Epoxy properties are shown in Table 2.2. After curing, the rods were ground flush with the faceplates. Figure 2.2a shows a completed sample. Using this method, single unit cells were fabricated with relative densities of 0.1, 0.6, 0.9, 1.6, 2, 2.5 and 3%. These were tested in compression at a maximum strain rate of $3 \times 10^{-4} \text{s}^{-1}$.

Table 2.1 CFRP sandwich panel component properties (33m.s.i fiber)

	Tensile Strength	Compressive Strength (MPa)	Flexural Strength (MPa)	Resin Matrix	Density g/cm^3
Pultruded rod	1379 MPa	820 MPa	1585.8	vinylester	1.49
Faceplate laminate	1220 MPa	335 MPa	1328	vinylester	1.44

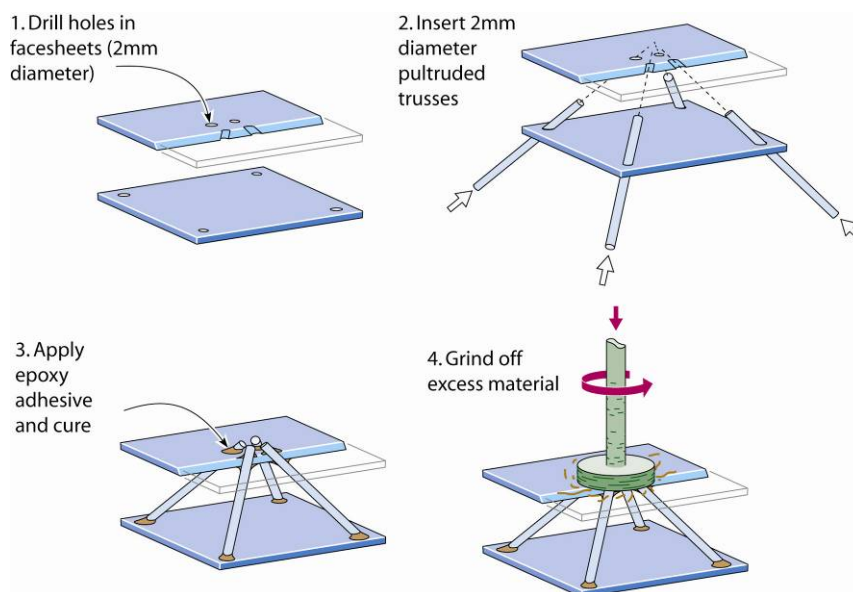


Fig. 2.1) Four step pultruded rod pyramidal core fabrication process. The holes in step one are hand reamed after drilling to accommodate the trusses for a tight mechanical fit.

Table 2.2 Fibreglast 2000/2060 Epoxy properties

Tensile Strength	Tensile Modulus	Flexural strength	Flexural Modulus	Strain to Fracture	Specific gravity
311 MPa	18 GPa	429 MPa	17.7 GPa	1.98%	1.11

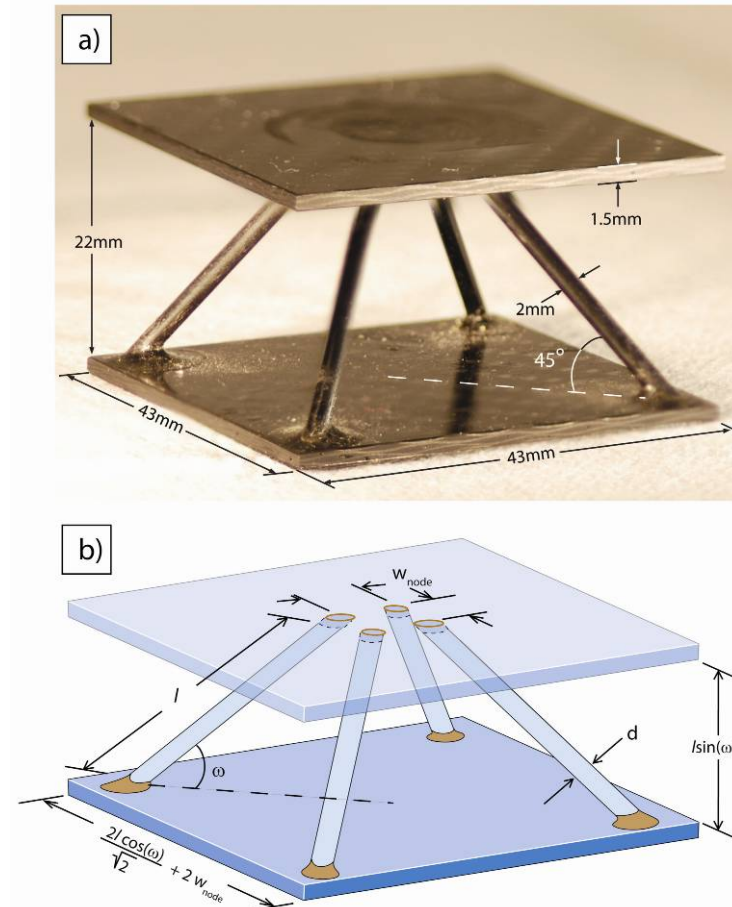


Fig. 2.2) Single cell pyramidal truss core. a) Completed sample using pultruded rod as ligaments $\bar{\rho} = 1\%$. b) Sketch of cell geometry and relevant variables.

The unit cell geometry is shown in Figure 2.2b. The length of the truss, l , is defined as the interior length and does not include the portion running through the facesheet. The node spacing, w_{node} , is the length from the center of a truss to the center of the adjacent truss at the node. The relative density for the pultruded cores follow as:

$$\bar{\rho} = \frac{\pi d^2}{2(l \cos(\omega) + \sqrt{2} w_{node})^2 (\sin(\omega))} \quad (2.1)$$

For all samples made using the method described here, $d=2\text{mm}$, $w_{node}=6\text{mm}$, and $\omega=45^\circ$. Relative density was varied by changing the truss length.

2.2 Results

The stress-strain response is shown in Figure 2.3 for representative individual tests. For all relative densities above 0.1%, panel failure was brittle. The strength of the panels dropped sharply after the samples reached a peak load. Peak strength increased with $\bar{\rho}$. A non-dimensional strength coefficient, $\Sigma = \sigma_p / (\sigma_{\max} \bar{\rho})$ is obtained by scaling the core peak compressional strength, σ_p , with respect to the compressional strength of the solid rod, σ_{\max} , and the relative density. This strength coefficient is a measure of the structural efficiency of the core in compression and it is plotted against relative density in Figure 2.4. The best structures reached an efficiency factor, Σ , of almost 0.3 but the average efficiency of this design is 0.16. The maximum theoretical efficiency for a pyramidal core is 0.5 [40]. Scatter in the data is indicative of the high sensitivity of the single cell tests to imperfections. Some samples tested did not have perfectly parallel faceplates which when compressed, resulted in some trusses experiencing larger stresses than others.

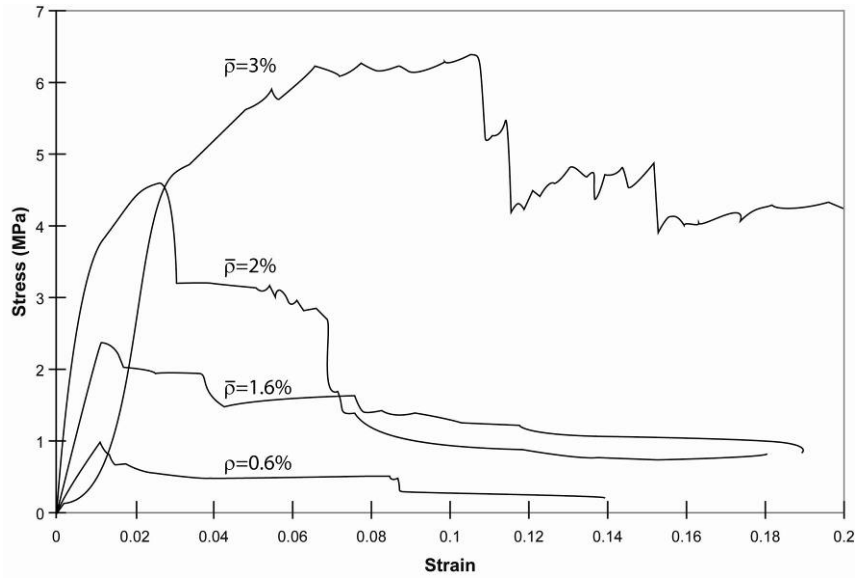


Fig. 2.3 Stress-strain response curves for several core relative densities

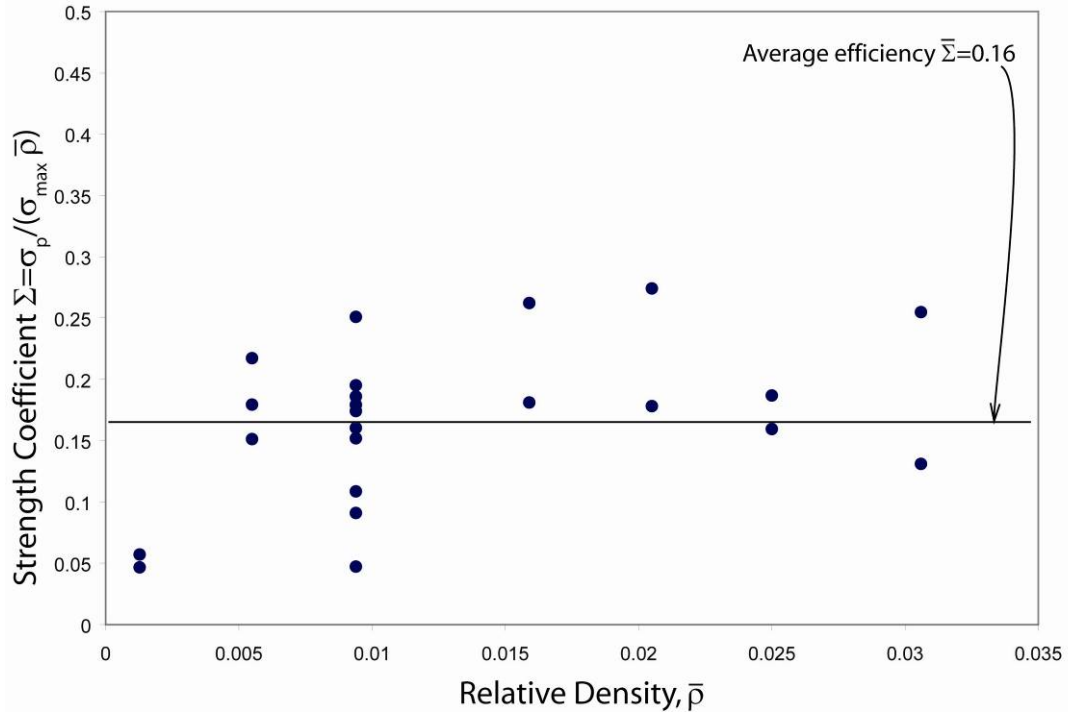


Fig. 2.4 Strength coefficient vs. relative density graph.

All samples tested except the lowest 0.1% relative density samples failed by a truss push-out mode in which the truss-facesheet interface failed in shear as shown in Figure 2.5b. Some of the higher relative density samples formed microbuckling kinks bands after node failure and truss push-out shifted the geometry of the unit cell shown in

Figure 2.5a. Truss push-out failures indicate a shortcoming in design as the strength of the panels depend on node strength and do not reflect the maximum strength attainable through truss failure.

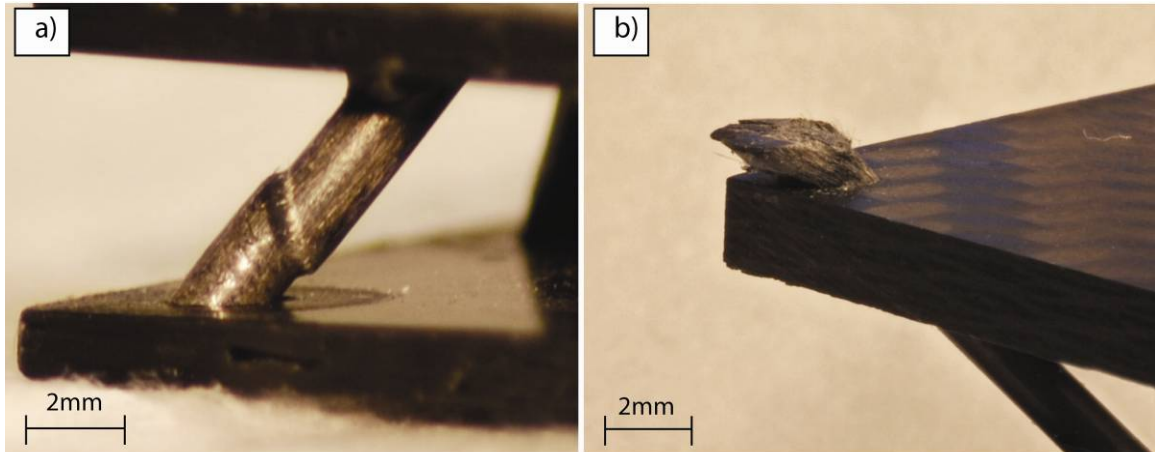


Fig. 2.5 Failure mechanisms in pultruded rod core. a) truss microbuckling, $\bar{\rho} = 3\%$. b) node push through (epoxy shear failure) $\bar{\rho} = 1\%$.

2.3 Discussion

The operative failure mechanism in the absence of elastic buckling (seen only in the 0.1% case) is truss push-out. The diagram shown in Figure 2.6 illustrates the forces present at the node ignoring bending. The axial force in the truss, F_a , is balanced by the shear force at the node, F_n , as long as the truss or epoxy bond does not fail.

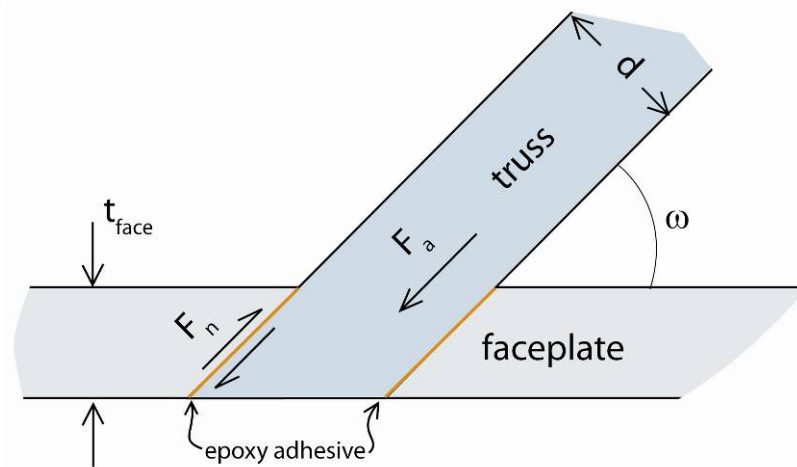


Fig 2.6 close-up drawing of the truss/faceplate junction

As relative density increases, the shear force placed on the node adhesive increases. Considering the total vertical compression force, F , on the unit cell, the reaction forces in equilibrium can be related by:

$$F_a = \frac{1}{4} F \sin \omega = F_n = \frac{t_{face}}{\sin \omega} \pi d \cdot \tau_a \quad (2.2)$$

Where t_{face} is the facesheet thickness and τ_a is the epoxy shear strength. Consider that the pyramidal core strength, σ_p , is related to F by:

$$\sigma_p = \frac{F}{2(l \cos(\omega) + \sqrt{2}w_{node})^2} = \frac{F \bar{\rho} \sin \omega}{\pi d^2} \quad (2.3)$$

Combining eqns. (2.2 and 2.3), the peak strength for the pyramidal unit cell as a function of relative density and adhesive shear strength, τ_a , follows as:

$$\sigma_p = \left(\frac{t_{face}}{d \sin(\omega)} \right) \tau_a \bar{\rho} \quad (2.4)$$

It is seen from the above relation that as relative density increases, the adhesive shear strength needed to prevent truss push-out increases. The strength of the panels produced

using this method is therefore limited by available adhesives and not by the material strength of the pultruded rod trusses.

Chapter 3 Unidirectional Laminate Fabrication Approach

3.1 Manufacturing method

The second design approach sought to prevent truss push-out at the nodes. Unidirectional carbon fiber laminates were obtained from Graphitestore.com (Buffalo Grove, IL). They were made using 228GPa (33m.s.i.) carbon fibers in a vinylester matrix with $v_f=60\%$. Laminate properties are given in Table 3.1. The laminate thickness was 1.5mm. The intent here was to create a mechanical and adhesive connection between trusses and the facesheets. Cross shaped slots were milled into the 3mm thick facesheet to a depth of $h_{tab}=1.5\text{mm}$ which was also one half the facesheet thickness. Individual truss elements with square cross-sections were then waterjet cut using the cutout pattern is shown in Figure 3.1.

Table 3.1 Unidirectional Laminate Properties (33 m.s.i fiber)

Tensile Strength	Flexural Strength	Compressive Strength	Density
2689 MPa	1875.4 MPa	540 MPa	1.49 g/cm ³

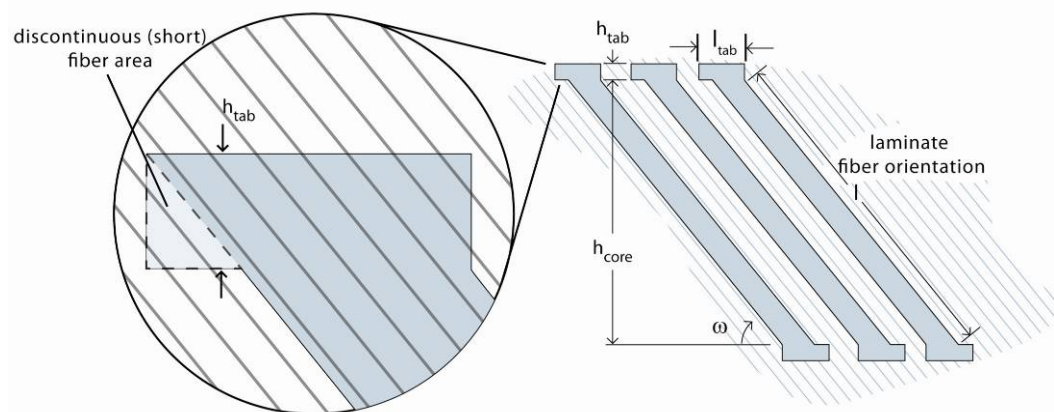


Fig. 3.1 Unidirectional laminate cut out pattern. The discontinuous fiber area is noted for being a potential weak point as it sheared from the truss, initiating node failure in some cases.

The tab height and length is h_{tab} and l_{tab} respectively. The truss inclination angle is ω . The truss length, l , and core height, h_{core} , are varied to give different relative densities while maintaining a constant truss cross-section.

The assembly process is shown in Figure 3.2a. The trusses were laid up individually with four discrete truss elements meeting at each node and epoxied into the facesheet slots. The epoxy used was Hysol EP-120 and its properties are given in Table 3.2. A photograph of an assembled core minus the top facesheet is shown in Figure 3.2b.

Table 3.2 Hysol EP-120 Epoxy Properties

Tensile Strength	Shear Strength	Elongation	Specific Gravity
41 MPa	20 MPa	10%	1.1

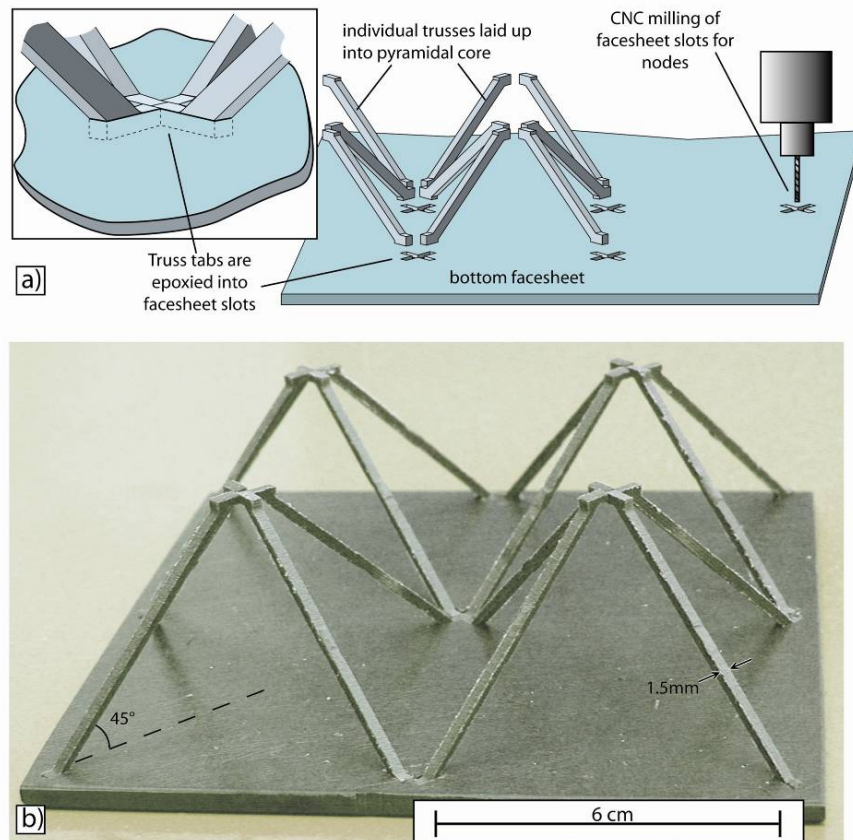


Fig. 3.2 Unidirectional laminate pyramidal core. a) assembly process and b) picture of completed 2x2 unit cell core with top facesheet removed $\bar{\rho} = 0.5\%$.

Sandwich panels were constructed consisting of four unit cells arranged in a 2x2 cell array (as in Figure 3.2b). Samples with core relative densities of 0.1, 1, 3.5 and 5% were fabricated and tested in compression. The unit cell geometry is shown in Figure 3.3. The tab height, h_{tab} , is not accounted for in the relative density calculation since it is fully buried in the facesheet in the completed panel and therefore not part of the core. The relative density for the core follows as:

$$\bar{\rho} = \frac{2tw}{\left(l \cos(\omega) + 2l_{tab} + \frac{t}{2} - \frac{w}{\sin(\omega)} \right)^2 (\sin(\omega))} \quad (3.1)$$

See appendix A for derivation. In all the samples created using this method, $t = w = 1.5\text{mm}$, $l_{tab} = 3.6\text{mm}$ and $\omega = 45^\circ$.

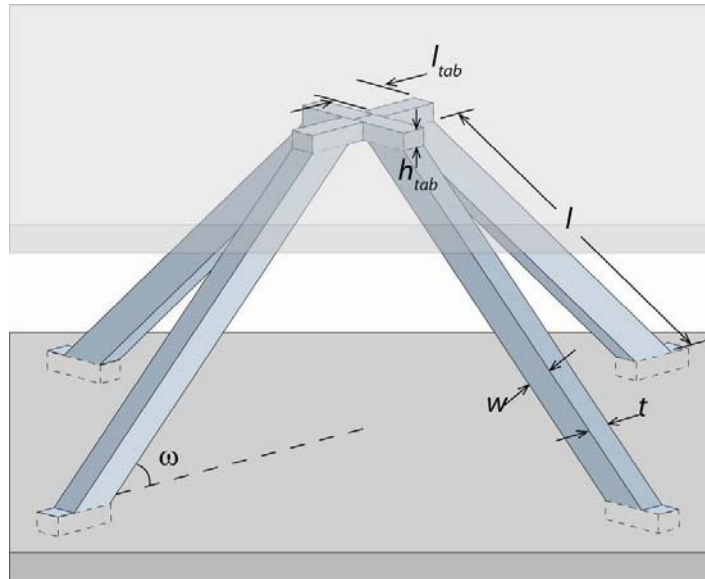


Fig. 3.3 Unidirectional laminate core unit cell geometry.

3.2 Results

Stress strain curves for representative tests are shown in Figure 3.4. Core failure occurred primarily at the nodes. Peak strength increased with $\bar{\rho}$, but the relationship does not appear to be linear. For the 0.1% relative density samples, elastic buckling was

observed to be the operative failure mechanism. The trusses would bend and finally break near the center of the beam where the bending stresses are highest as shown in Figure 3.5a. The non-dimensional strength coefficient is plotted against relative density in Figure 3.5. At 1% relative density and higher, the discontinuous fiber area detailed in Figure 3.1 tended to shear off of the trusses and initiate node failure. This mechanism is shown in Figure 3.6b and was seen to occur in the node center where trusses pushed into each other. As forces on the trusses increase with increasing relative density, this node failure mechanism became dominant. The drop in structural efficiency seen in Figure 3.5 is reflective of the change in failure modes. Only a few tests were performed using this second design as it became apparent that while push out failure at the node was defeated, an even weaker failure mechanism was active at the nodes making it impossible to achieve the potential strength of the core.

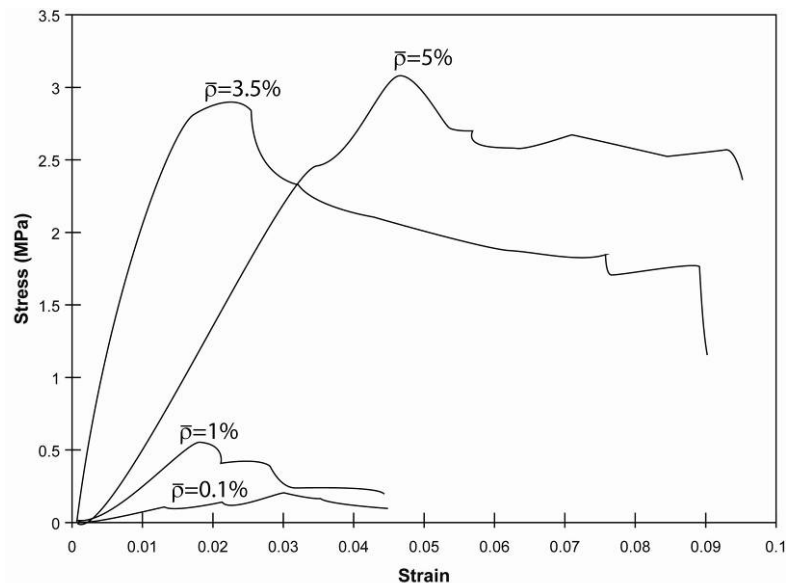


Fig. 3.4 Stress-strain response for unidirectional cores over a range of relative densities

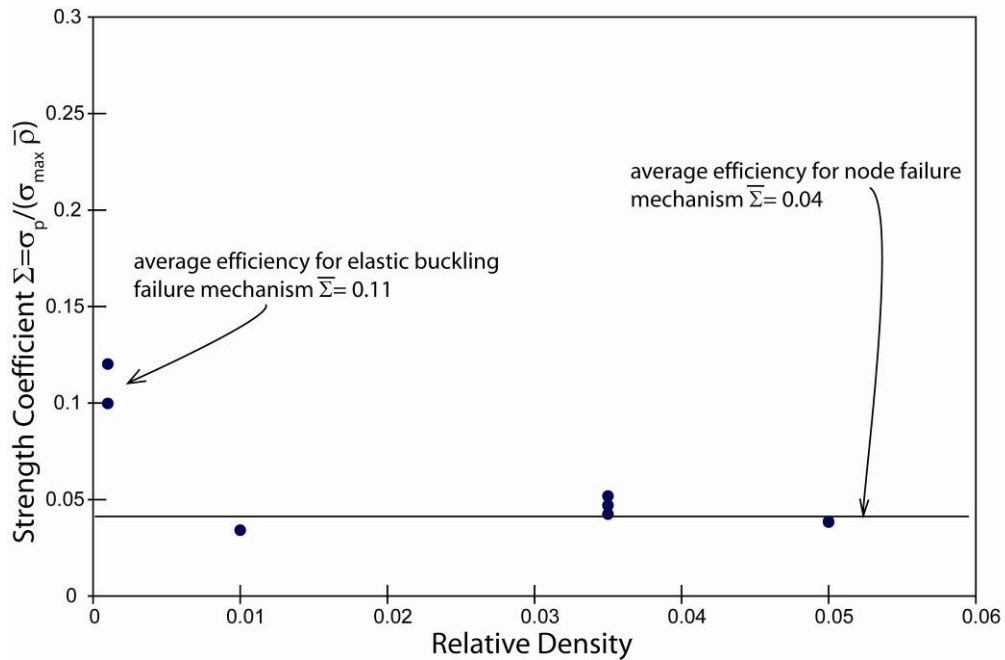


Fig. 3.5 Strength coefficient vs. relative density chart for unidirectional laminate core.

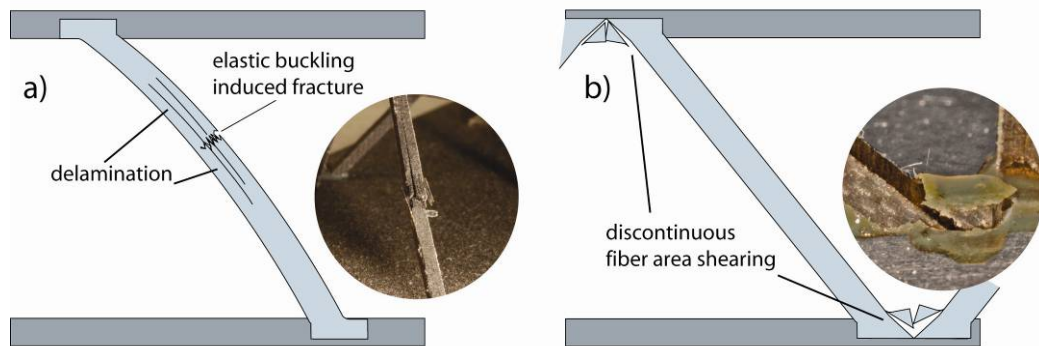


Fig. 3.6 Failure mechanisms for unidirectional laminate trusses. a) Mid-truss fracture due to elastic buckling. b) Internal node failure by shearing of fibers discontinuous with respect to the truss.

3.3 Discussion

This method of construction proved somewhat easier to implement and was less susceptible to imperfections and misalignments. The use of milled slots prevented truss push through and multiple unit cells ensured the top facesheet was level. While these design improvements helped during construction, the strength of the cores were less than

the pultruded rod cores from Chapter 2. Though the trusses were better constrained, node failure was still present and decreased the structural efficiency significantly.

Chapter 4 Bi-Directional Laminate Fabrication Method

Node design is of critical importance as evidenced by the node failure mechanisms in Chapters 2 and 3. Generally stronger core designs require stronger nodes at the truss-facesheet junction. The milled-slot method of node constraint, used in Chapter 3, prevented node push-out failure but allowed a new type of failure due to discontinuous fiber shear at the nodes. We note that by using a biaxial laminate and connecting the trusses together as shown in Figure 4.1b, the discontinuous fiber areas can be reinforced with crossing fibers which might inhibit node shearing. The third design approach used a modification of the method in Chapter 3 to implement this observation. It also represented a significant improvement to the assembly process. The method was based upon the orthogonal snap fitting of 2-D truss rows cut from bi-axial CFRP laminate panels. Any non-ductile material may be formed into pyramidal core structures by cutting slot-fit truss patterns from a sheet using this method. Figure 4.1 shows the manufacturing process. Continuous 2-D truss patterns eliminated the need to orient trusses individually and therefore cut down on misalignments and allowed for faster assembly.

Fibrous composite laminates are highly anisotropic with their highest strength lying in the direction of the fiber axes. The truss cut-out patterns were aligned with the laminate fiber axes so as to give the trusses the highest strength as shown in Figure 4.1a,b. The laminate plies were laid up in an alternating 0/90° fashion. Any lay-up angle may be used however, the 0/90° configuration is the most common for biaxial laminates [41].

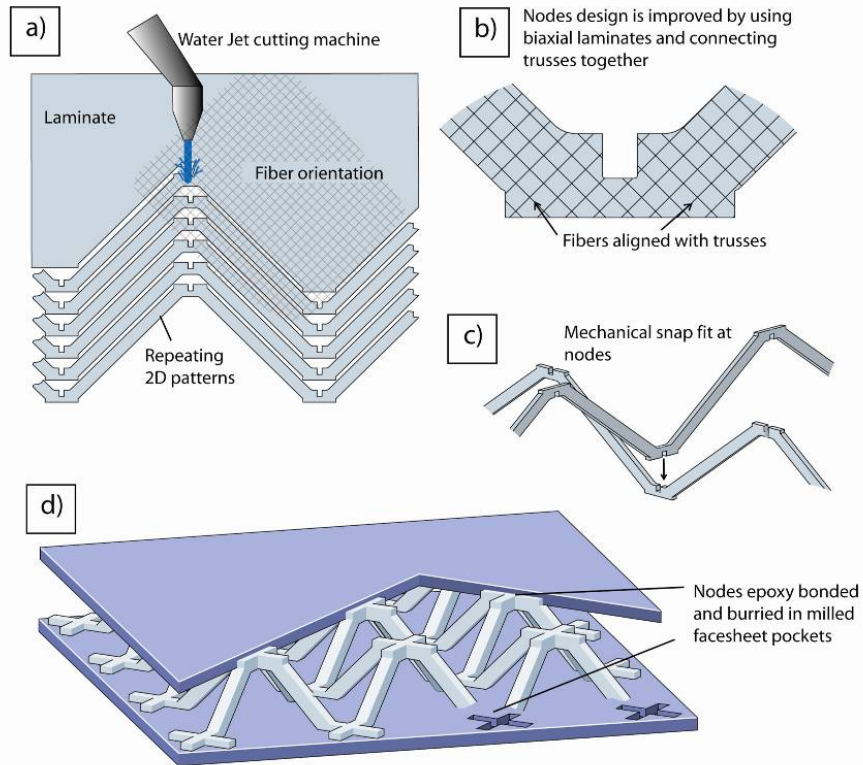


Fig. 4.1) Manufacturing and assembly process. a) Continuous 2-D truss elements were cut from the laminate via water-jet. b) Use of biaxial laminates reinforce the node. c) The patterns are snap fit together at nodes. d) The cores were epoxy bonded to the facesheet with node tabs counter-sunk into milled slots.

The ideal pyramidal structure seeks to minimize the material at the node since this part of the core does not contribute to the strength of the truss. In practice, bulkier nodes are necessary to ensure adequate facesheet attachment and to prevent premature failure at the nodes. Two designs were investigated in order to determine the effect of node width on panel performance. The cutout pattern and core geometry are shown in Figure 4.2. The parameters for the two designs are listed in Table 4.1. Design 1 used a small node volume while design 2 increased the contact surface area but at the cost of “wasted” node mass.

Table 4.1 Core design parameters

	ω	h (mm)	t=w (mm)	b (mm)	c (mm)
Design 1	45°	3	3	6.4	3.8
Design 2	45°	1.6	3	15.3	9.6

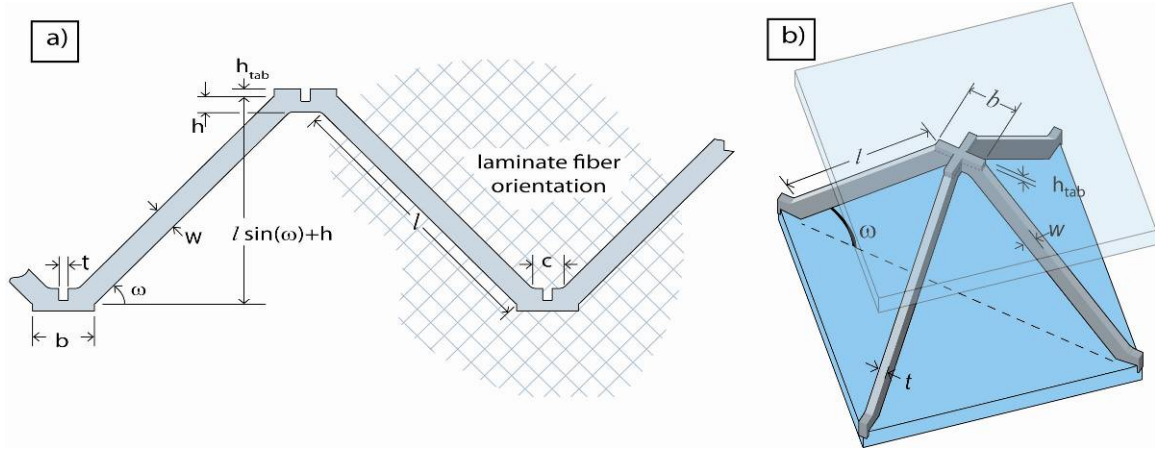


Fig. 4.2 Core geometry and variables. a) 2D view of the laminate cutout pattern b) Isometric view of a unit cell

In calculating the relative density, the node tab height, h_{tab} , is not included as the tab becomes part of the face plate in the completed panel and so is not considered part of the core. The relative density is then written:

$$\bar{\rho} = \frac{2 \left[ltw + \frac{1}{2} ht(b+c-t) \right]}{(l \sin(\omega) + h) \left(l \cos(\omega) + \frac{1}{2} (b+c) \right)^2} \quad (4.1)$$

See Appendix B for derivation. For all experiments in this study, $w=t$ in order to prevent the occurrence of preferential buckling or twisting failure modes in the trusses. All the cores fabricated using this method had a constant cross section of 3mm and, as a result, the cell height varied with relative density. The truss lengths and corresponding relative densities are shown in Table 4.2. Due to the wider node length, design 2 cores had a lower cell height compared with design 1 for a given relative density. Design 1 panels

were fabricated with relative densities of 1, 2, 3.5 and 5% while design 2 panels were made with relative densities of 3.5, 5, 7 and 10%. The two node designs are shown in Figure 4.3.

Table 4.2 list of truss lengths and corresponding relative densities

	Design 1		Design 2	
	$\bar{\rho}$	$l(\text{mm})$	$\bar{\rho}$	$l(\text{mm})$
	0.01	65.8	0.03	28.3
	0.02	43.9	0.05	18.7
	0.035	31.6	0.07	13.7
	0.05	24.6	0.10	9.4

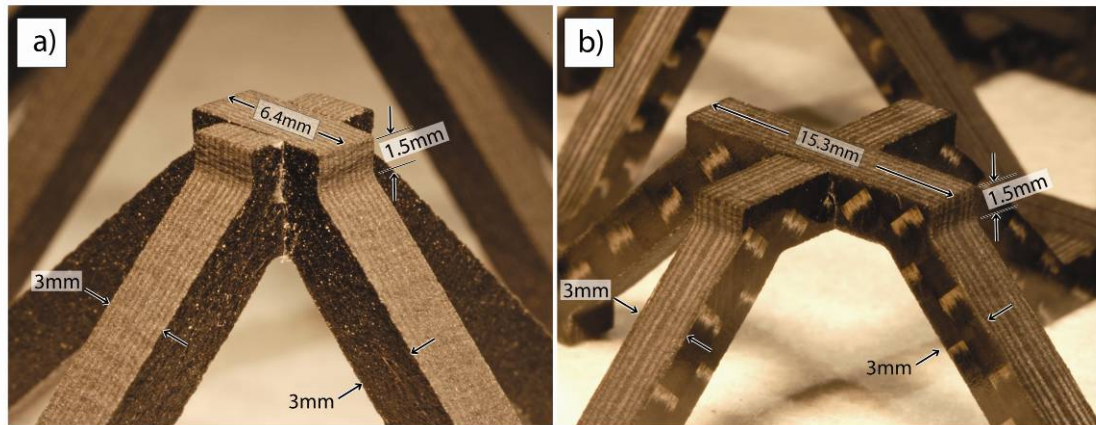


Fig. 4.3 Two node designs. a) design 1 minimizes node width $\bar{\rho}=3.5\%$ b) design 2 uses larger surface area in attempt to increase node strength $\bar{\rho}=7\%$. Wider nodes also decrease core height for a given relative density.

Truss patterns were machined using an abrasive water-jet with beam diameter of 0.5mm. The small beam diameter makes efficient use of the polymer laminate; by stacking the cut-out pattern as in Figure 4.1a, most of the original laminate plate ends up in the completed structure. Another benefit of the water jet is that unlike most other machining methods it does not produce heat, which can damage the matrix material at the cut edge. The truss patterns were assembled and epoxy bonded to the facesheets at the nodes using Hysol EP-120 epoxy. See Table 3.2 for adhesive properties. The milled

facesheet slots were cut to a depth $h_{tab} = 1.5\text{mm}$. A completed panel is shown in Figure 4.4.

Due to fiber shortages, two different companies supplied laminates used to create the cores for this study. Graphitestore.com (Buffalo Grove, IL) manufactured the panels used in Design 1. Hexcel M10 laminates supplied by McMaster-Carr (Atlanta, GA) were used to make Design 2 panels. In both cases, the laminates used were made from 228GPa (33 m.s.i.) carbon fibers laid up in unidirectional plies in an alternating 0-90° orientation. Ply thickness varied between laminates but the total laminate thickness was 3mm for both designs. Table 4.3 lists the laminate specifications. The laminate material properties, σ_{\max} and E_s , are the maximum compressive strength and the compressive modulus taken to be in-plane and parallel to the fiber axis. Laminate 1 was used for Design 1 cores and laminate 2 was used in Design 2 cores.

Table 4.3 Laminate architecture and properties

	#plies	Lay-up	Matrix	v_f	Density	σ_{\max}	E_s
Lam 1	24	[0,90] _s	vinylester	55%	1.44 g/cm ³	611MPa	24.2GPa
Lam 2	14	[0,90] _s	epoxy	55%	1.5 g/cm ³	615MPa	29.1GPa

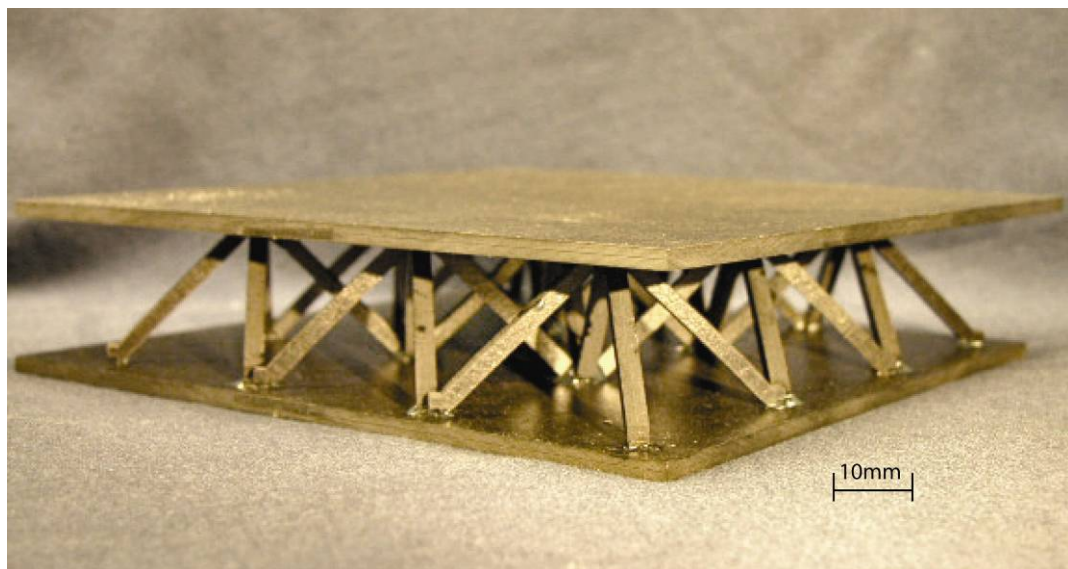


Fig 4.4 Completed pyramidal core sandwich panel. Design 1 $\bar{\rho} = 3.5\%$

This method of fabricating pyramidal lattice structures from bi-axial laminates overcomes the inadequacies of previous methods. Improvements to node design and assembly process sufficiently constrain core failure to the truss members and allow the relationship between bulk material and core strength properties to be examined. However, this was achieved at the expense of having only 50% of the fibers in the truss load support direction and significant inefficiency due to the node parasitic mass.

Chapter 5: Mechanical Testing Methodology

Three types of tests were carried out in order to characterize the material response of the two pyramidal CFRP lattice panel designs described in Chapter 4. Transverse compression tests were used to measure the structural stiffness and strength of the panels over a range of relative densities. Uni-axial clamped compression tests were performed on the parent laminate in order to determine the individual truss material properties. Unclamped edge-wise tests were also carried out in order to estimate the compressive strength of the two laminate materials. Obtaining the laminate properties allows comparisons to be made between the two core/node designs (since different laminates were used) and was necessary for comparisons with micromechanical models described later.

5.1 Pyramidal lattice compression tests

A servo driven universal testing machine (Model 4208, Instron Corp., Canton, MA) was used to perform transverse compression tests on the sandwich panels at a compression rate of 0.003mm/min per mm core height, in accordance with ASTM C-365 standard. Table 5.1 gives the sample core heights and resulting strain rates. A laser extensometer was used to monitor the compressive strain of the sample via retro-reflective tabs placed on the edges of the face sheets. Stress was computed by dividing the peak force by the area of the core base defined by the centers of the outer edge nodes. The experimental setup is shown in Figure 5.1. The nominal macroscopic core strain is

defined as the load cell displacement divided by the original sandwich panel thickness. Tests were carried out on Design 1 panels at four relative densities: 1, 2, 3.5 and 5% with five samples tested at each density. Design 2 panels were tested at 3, 5, 7, and 10% again with five samples at each density. The number of unit cells included in each sample varied with relative density to ensure that the sample size was appropriate for the limitations of the equipment. Panels with relative densities at 3% and below were made using a 2x2 unit cell core. At 3.5% relative density and higher, the test panels used a 3x3 unit cell core.

Table 5.1 Compression test strain rates

$\bar{\rho}$	Design 1 core height (mm)	strain rate s^{-1}	$\bar{\rho}$	Design 2 core height (mm)	strain rate s^{-1}
1%	50	5×10^{-5}	3%	22	4.5×10^{-5}
2%	34	5×10^{-5}	5%	15	4.4×10^{-5}
3.5%	25	5×10^{-5}	7%	11	4.5×10^{-5}
5%	20	5×10^{-5}	10%	8	4.1×10^{-5}

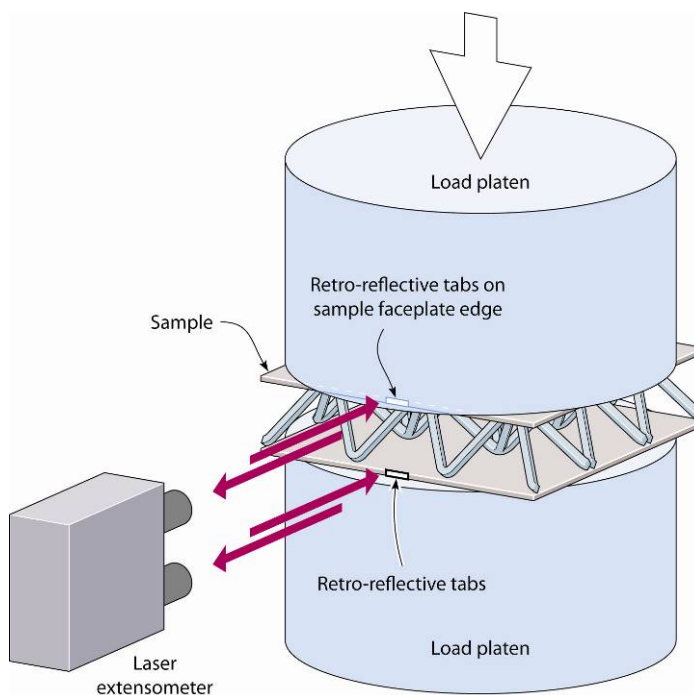


Fig. 5.1 Experimental setup of through-thickness compression tests.

5.2 Laminate compression tests

It is difficult to reliably test fibrous composites in compression [42]. Testing standards have undergone several revisions over the past decade as the use of fibrous composites in critical applications has increased [43]. Unlike isotropic materials, end clamping forces can produce undesirable stresses in the gauge section of the composite test specimen. Even when clamping stresses are reduced, the end conditions affect the failure strength of the laminate as different failure modes are being activated. In an effort to produce compression data for the laminates spanning the end conditions present during testing of the lattice core panels, two types of tests were carried out.

5.2.1 Combined Clamped/End Loading Tests

The clamped laminate response was tested using a combined load compression (CLC) test according to ASTM D-6641 standard. Straight rectangular coupons were milled from the laminates using a CNC machine. The test rig, shown in Figure 5.2, is designed to compressively load a specimen through the combination of shear (clamping screws) and end loading. Compression was administered at a strain rate of $5 \times 10^{-4} \text{s}^{-1}$. A laser extensometer measured the test specimen strain by retro-reflective tabs placed on the loading rig as shown in Figure 5.2. Six samples were tested for each laminate. This test method gives the upper bound strength for the laminates as the clamping inhibits interply delamination at the strut ends.

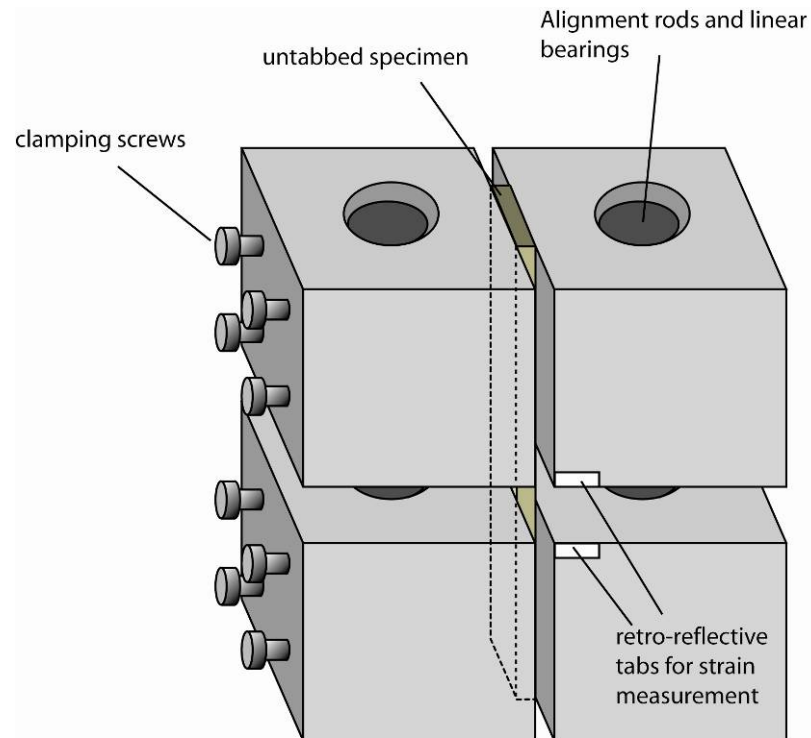


Fig. 5.2 Combined Loading Compression (CLC) test rig. The untabbed specimen is positioned flush with the top and bottom of the rig. Clamping forces provided by the screws are combined with end loading as the rig is compressed in an Instron test machine.

5.2.2 Unclamped compression tests

Compression tests for bi-axial laminates under clamped conditions fail by microbuckling of the 0° plies. The clamps forcibly prevent a delamination failure which is active when no clamping is present. In order to determine the delamination strength, unclamped compression tests were performed on the two laminates. Small rectangular samples ($3 \times 12.5 \times 19.5 \text{ mm}$) were carefully milled to ensure flat, parallel load ends. The samples were then placed directly on the load platens of the Instron testing machine with a gauge length between the platens of 12.5mm. Edge-wise compression loading was administered at a strain rate of $5 \times 10^{-4} \text{ s}^{-1}$. Strain data was measured by laser extensometer.

Chapter 6:

Biaxial Laminate Results

First we report the parent laminate properties and then examine the core responses for the two designs.

6.1 Laminate Properties

The two laminates used to create the different node/core designs were tested in axial compression with and without clamped end conditions. The results of the tests are summarized in table 6.1. Stress strain curves for individual tests are shown in Figure 6.1. The specimens were periodically unloaded and reloaded during testing to obtain the compressive stiffness, E_s , of the laminates; defined as the slope of the line passing through the two pointed ends of the unload/reload loop. It is noted that the laminates exhibit plastic behavior during the clamped compression tests as evidenced in the progression of the residual strain of the unloading curves in Figure 6.1a,b. Unclamped tests in Figure 6.1c,d reveal an elastic response as well as retaining some post failure strength not seen for the clamped response, providing evidence that different failure mechanisms are active in the two tests.

Table 6.1 Summary of results from in-plane laminate compression tests for clamped (CLC) and unclamped end conditions

	σ_{\max} MPa	std dev of σ_{\max} MPa	E_s GPa	std dev of E_s GPa
Laminate 1 (clamped)	611	34	24.185	0.865
Laminate 1 (unclamped)	380	129	27.612	5.390
Laminate 2 (clamped)	615	41	29.122	0.619
Laminate 2 (unclamped)	357	108	28.481	4.350

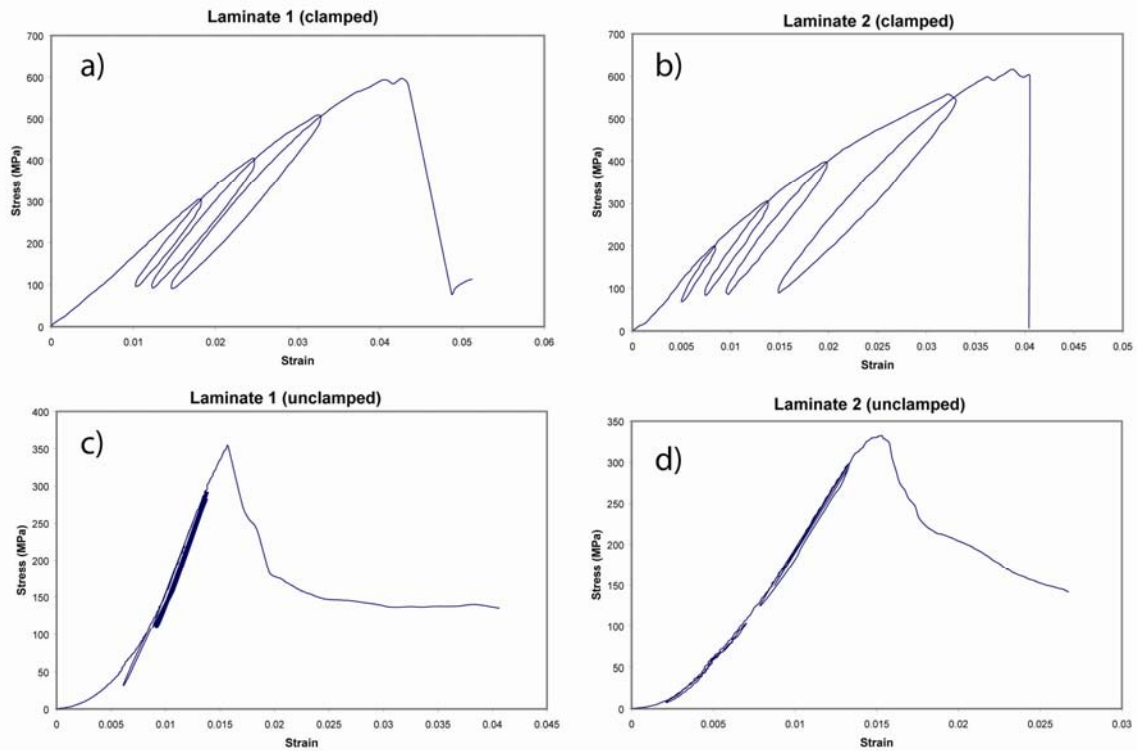


Fig. 6.1 Compressive stress strain response curves for two laminates under a,b) clamped and c,d) unclamped conditions.

During clamped tests, audible crackling in the specimens was observed prior to catastrophic failure which was accompanied by a loud “pop”. Figure 6.2 shows the specimen failure zones. The span of time between crackling and total failure is on the order of half a second. One test specimen was preserved after crackling but before total failure. Under an optical microscope, this sample gives visual confirmation of localized fiber microbuckling in the 0° plies shown in Figure 6.2c,d.

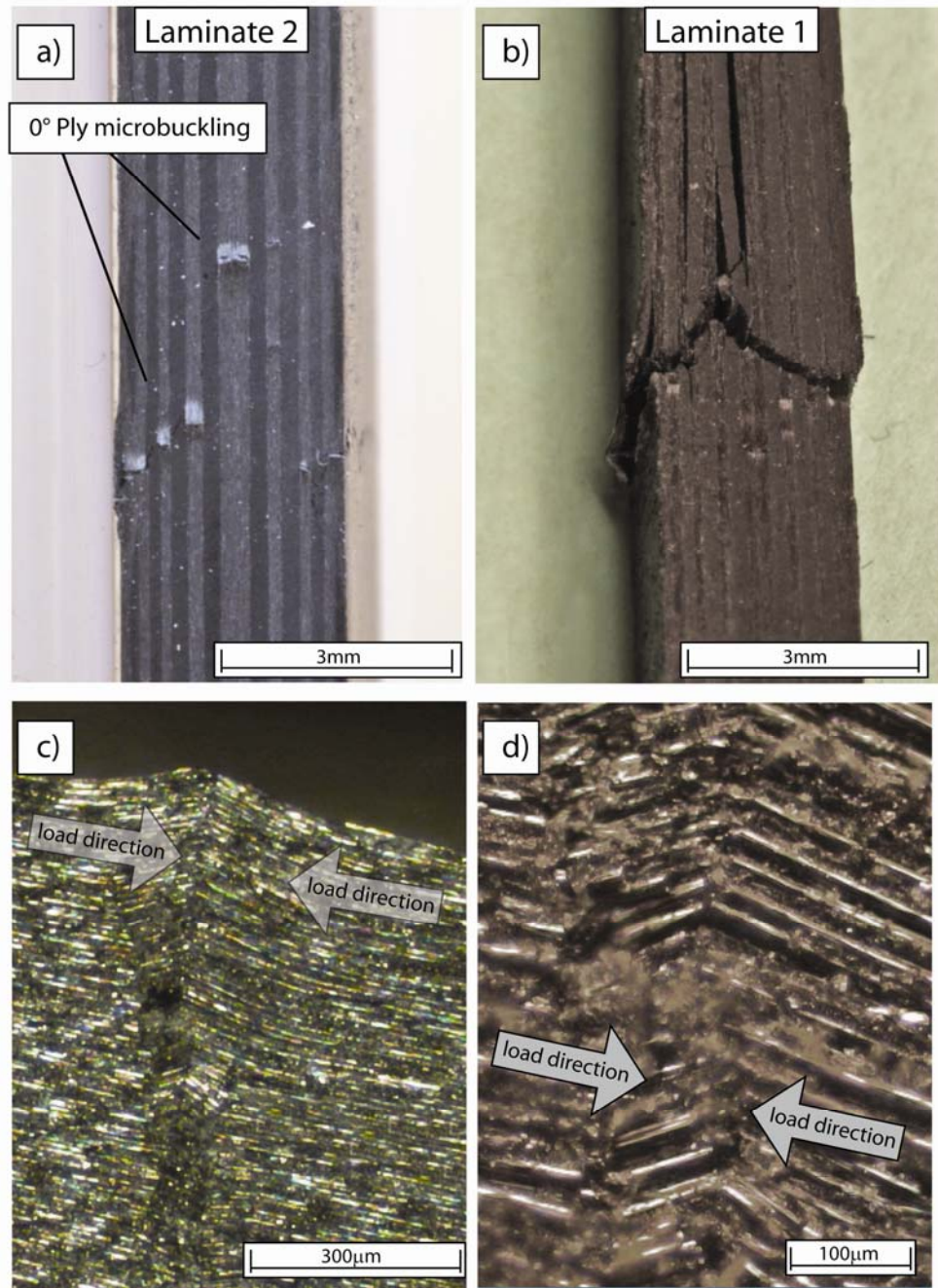


Fig. 6.2 Failure zones for clamped laminate compression tests. a) Laminate 2 just before failure, 0° plies undergo microbuckling and cause delamination and shearing in the 90° plies. b) Laminate 1 after catastrophic truss failure occurs. c,d) microscope view of specimen in a) at localized fiber microbuckling sites

Unclamped specimens failed by delamination following a slight brooming at one end. Post failure specimens are shown in figure 6.3. The delamination failure mode is weaker than a microbuckling mode of failure by approximately 300 MPa, Table 6.1

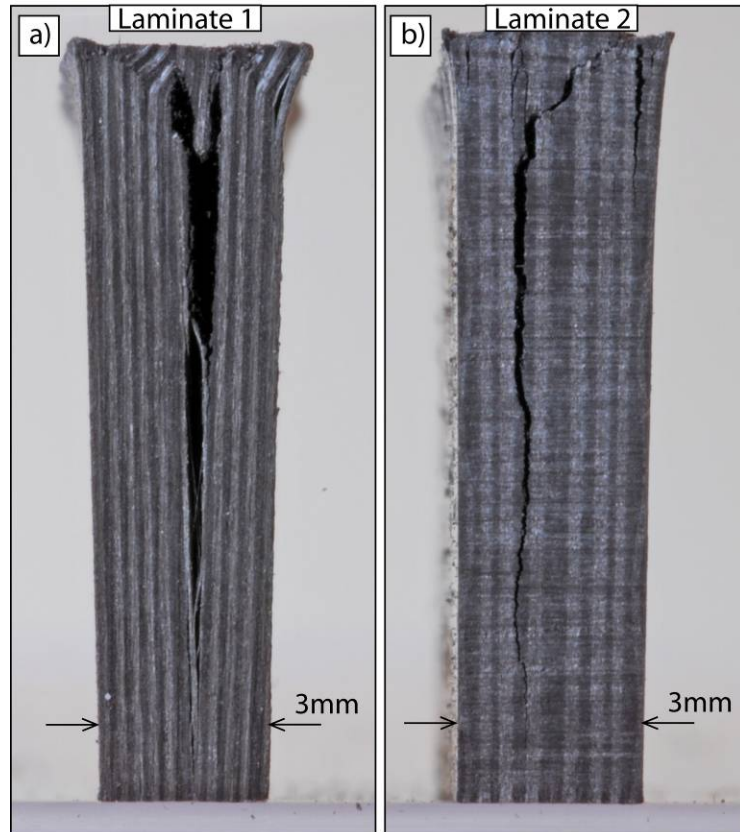


Fig. 6.3 Failure of unclamped compression tests. Delamination failure is preceded by slight brooming at one end of the test specimen. a) Laminate 1 b) Laminate 2

6.2 Pyramidal Core Compression Results

Pyramidal core sandwich panels were tested in through-thickness compression. The stress strain curves from the two cores are shown in Figure 6.4, where the reloading cycles have been removed for clarity. Both core designs behaved plastically with increasing load. The through thickness panel stiffness, E_p , was calculated from the tests via unloading/reloading curves as described above. The compressive stiffness and peak strength are plotted against relative density in Figures 6.5.

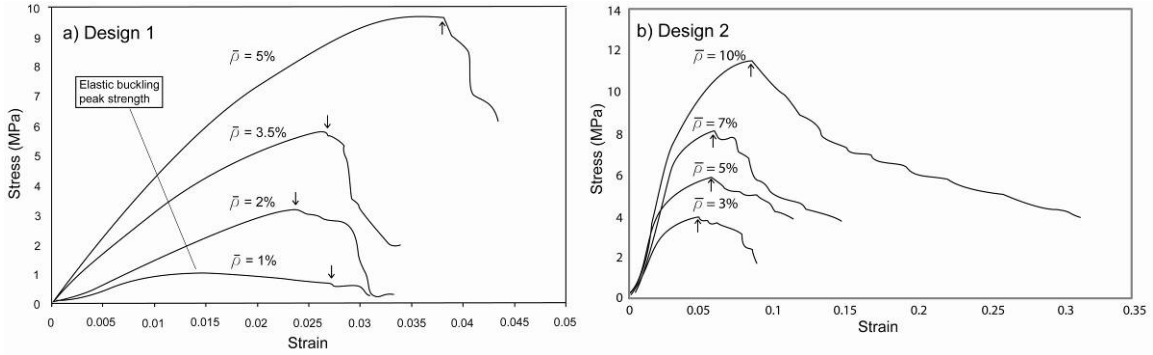


Fig. 6.4 Stress-Strain response for a) node/core design 1 and b) node/core design 2. Arrows indicate first observance of truss failure.

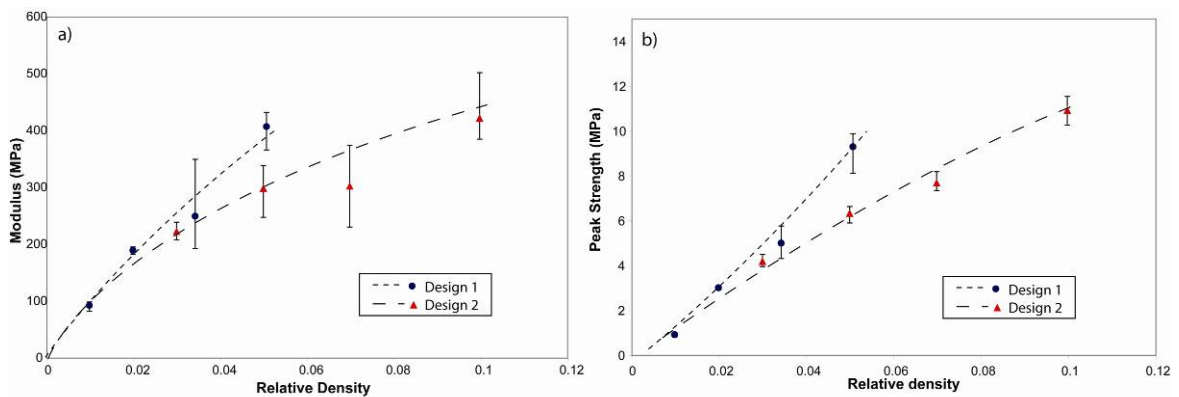


Fig. 6.5 Pyramidal core compression results. a) Modulus vs. relative density and b) Peak strength vs. relative density. Error bars reflect the maximum and minimum experimental values.

Compression tests were carried out until a number of trusses underwent failure. Small, sharp decreases in strength as indicated by the arrows in Figure 6.4, represent the first occurrence of catastrophic truss failure. Generally several trusses would fail in rapid succession causing the panel strength to drop dramatically. Audible crackling was observed prior to truss rupture. In nearly all cases, truss failure occurred where the truss connected to the node. This “ankle” failure is shown in Figure 6.6. Elastic “Euler” buckling was only seen in the 1% relative density case for Design 1. Figure 6.7 shows core member buckling during testing. During elastic buckling, the truss would visibly

bow until it ruptured at the center of the truss as seen in Figure 6.7b. For the 2% relative density cores, mid-truss failure was observed along with ankle failure.

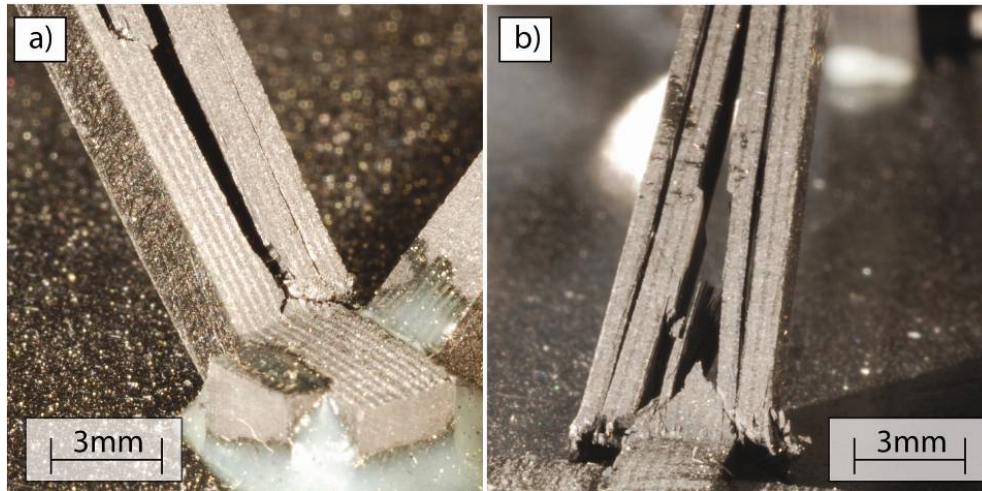


Fig. 6.6 Near-node truss fracture a) design 1 $\bar{\rho} = 3.5\%$ and b) design 2 $\bar{\rho} = 5\%$. This “ankle” fracture is the most common failure observed for the cores

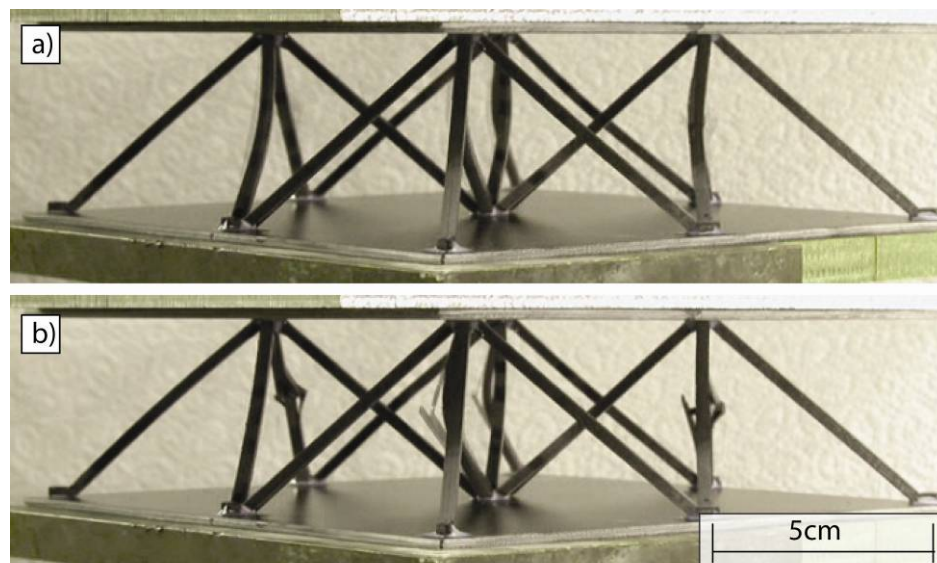


Fig. 6.7) Elastic Euler buckling failure for low relative density core $\bar{\rho} = 1\%$ a) peak strength of the core is determined by the onset of buckling b) failure occurs mid-truss where stress concentrations are highest.

Chapter 7

Micromechanical Modeling

In an effort to understand the behavior of the CFRP lattice structures, analytical expressions for the “effective” transverse compressive stiffness and strength of a pyramidal core sandwiched between two rigid face-sheets have been derived in collaboration with Professor Vikram Deshpande [44]. The pyramidal trusses are made from 0-90° laminates such that one set of fibers were aligned with the axial direction of the struts of the pyramidal truss. A local Cartesian co-ordinate system ($e_1 - e_2$) aligned with the orthogonal set of fibers was defined as in Figure 7.1a. The Young's modulus and compressive plastic micro-buckling strengths of the laminate in either the e_1 or e_2 directions are defined by E_s and σ_c , respectively while τ_y is the longitudinal shear strength of the matrix material used to construct the laminate.

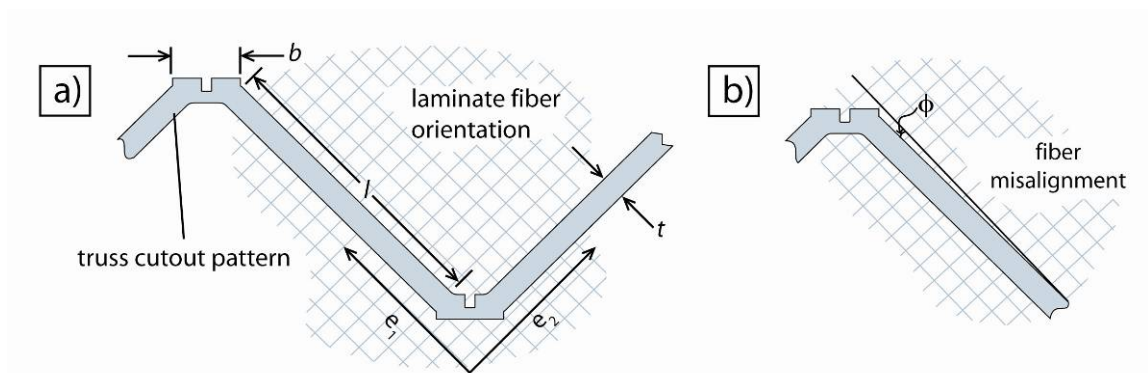


Fig. 7.1 Bi-axial laminate truss cut-out pattern. a) fiber orientation with local Cartesian coordinates aligned with the fiber axes. b) fiber misalignment angle

The maximum compressional strength of the laminate lies along the e_1 and e_2 directions. Misalignment of the fibers as shown in 7.1b can be created during the

fabrication process as the individual plies are laid up for laminating, or during machining when the panel is lined up for cutting. It is important to recall that the peak strength of laminates falls off quickly with increasing ϕ [41].

7.1 Elastic properties

In order to derive the compressive elastic modulus of the pyramidal core, E_p , in terms of the core geometry and the elastic properties of the solid material, an analysis of the elastic deformations in a single strut of the core is first carried out, and the results then extended to determine the effective properties of the entire core.

Consider an edge clamped strut of length l and square cross-section of side t as shown in Figure 7.2. This represents a single strut of the pyramidal core and thus symmetry considerations dictate that the top end of the strut is only free to move along the x_3 -direction. For an imposed displacement δ in the x_3 -direction the axial and shear forces in the strut are given by elementary beam theory [45] as:

$$F_A = E_s t^2 \frac{\delta \sin \omega}{l}, \quad (7.1)$$

and

$$F_S = \frac{12E_s I \delta \cos \omega}{l^3}, \quad (7.1)$$

respectively, where $I \equiv t^4/12$ is the second moment of area of the strut cross-section.

The total applied force, F , in the x_3 -direction then follows as:

$$F = F_A \sin \omega + F_S \cos \omega = \frac{E_s t^2 \delta}{l} \left[\sin^2 \omega + \left(\frac{t}{l} \right)^2 \frac{\cos^2 \omega}{\sin \omega} \right] \quad (7.2)$$

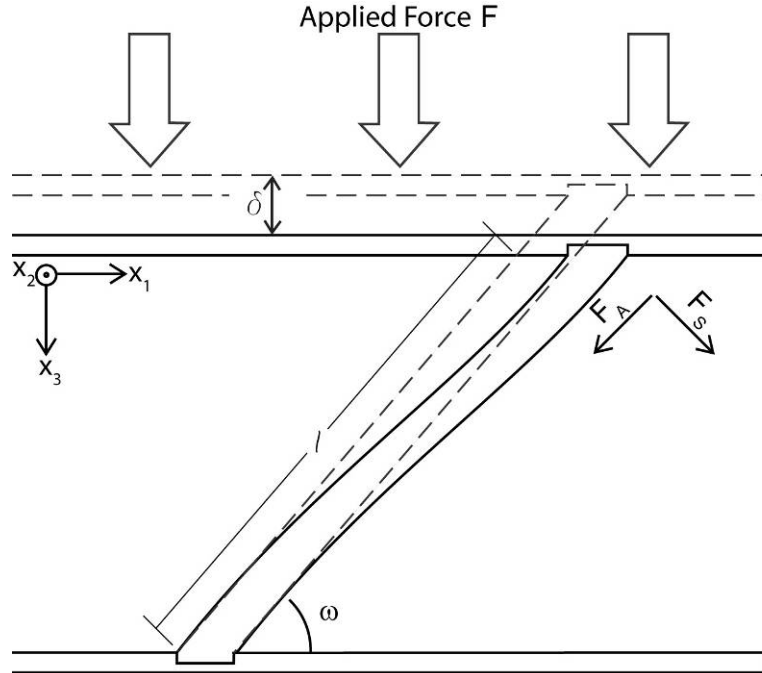


Fig. 7.2 Sketch of the deformation of a single strut of the pyramidal core under uni-axial compression

The applied through-thickness nominal stress σ and strain ε of the pyramidal core are then related to the force and displacement, δ , by:

$$\sigma \equiv \frac{8F}{(2l \cos \omega + 2b)^2}, \quad (7.3a)$$

and

$$\varepsilon \equiv \frac{\delta}{l \sin \omega}, \quad (7.3b)$$

respectively. The effective Young's modulus, $E_p \equiv \sigma / \varepsilon$, of the pyramidal core then follows from Eqs. (7.2) and (7.3) as:

$$\frac{E_p}{E_s} = \frac{2\bar{l} \sin \omega}{\bar{l}(\bar{l} \cos \omega + \bar{b})^2} \left[\sin^2 \omega + \frac{\cos^2 \omega}{\bar{l}^2 \sin \omega} \right] \quad (7.4)$$

Here, the modulus is given in terms of the non-dimensional geometric parameters of the core $\bar{l} \equiv l/t$ and node $\bar{b} \equiv b/t$. In the limit of negligible node volume (i.e. $b = h = c \rightarrow 0$), the modulus is related to the relative density $\bar{\rho}$ of the core via:

$$\frac{E_p}{E_s} \approx \frac{2 \sin \omega}{\bar{l}^2 \cos^2 \omega} \left[\sin^2 \omega + \frac{\cos^2 \omega}{\bar{l}^2 \sin \omega} \right] = \bar{\rho} \sin^4 \omega + \frac{\bar{\rho}^2}{2} \sin^2 \omega \cos^4 \omega \quad (7.5)$$

The first and second terms in Eq. (7.5) represent the contributions to the stiffness of the pyramidal core due to the stretching and bending of the struts, respectively.

7.2 Collapse strength

We consider the three critical collapse mechanisms for the pyramidal core: plastic micro-buckling of the composite struts; delamination failure of the struts and elastic Euler buckling of the struts. The operative failure mode is the one associated with the lowest value of the collapse strength. Typically polymer matrices of fiber composites display non-linear behavior [46] and thus elastic micro-buckling is not an operative failure mode and not considered in the collapse calculations presented here.

7.2.1 Plastic Micro-Buckling of the Composite Struts

It is generally accepted that fiber micro-buckling of composites is an imperfection-sensitive, plastic buckling event involving the non-linear longitudinal shear of the composite within a narrow kink band. Argon [47] argued that the compressive strength σ_{\max} for a composite comprising inextensional fibers and a rigid-ideally plastic matrix of shear strength τ_y , is given by:

$$\sigma_{\max} = \frac{\tau_y}{\phi}, \quad (7.6)$$

Kinking initiates from a local region of high fiber misalignment of angle $\bar{\phi}$. It is assumed that the micro-buckle band is transverse to the axial fiber direction e_1 , such that the angle β between the normal to the band and the fiber direction vanishes.

Now consider the case where the remote stress state consists of in-plane shear τ^∞ in addition to a compressive stress parallel to the fibers. Then, Fleck and Budiansky [48] have shown that:

$$\sigma_c = \frac{\tau_Y - \tau^\infty}{\bar{\phi}}. \quad (7.7)$$

Prior to micro-buckling of the struts, the struts are elastic and the analysis of Section 7.2.3 applies. Thus, from Eqs. (7.1) and (7.7) it follows that the axial stress σ_c required to initiate micro-buckling in the inclined strut sketched in Fig. 7.2 is given by:

$$\sigma_c = \frac{\tau_Y}{\left[\bar{\phi} + \cot \omega \left(\frac{t}{l} \right)^2 \right]} = \frac{\sigma_{\max}}{\left[1 + \frac{\cot \omega}{\bar{\phi}} \left(\frac{t}{l} \right)^2 \right]}, \quad (7.8)$$

where σ_{\max} is the micro-buckling strength of the laminate for loading in the e_1 -direction in the absence of remote shear. Taking into account that the unit cell of the pyramidal core comprises of four such struts, the nominal through thickness compressive strength of the pyramidal core is then given as:

$$\sigma_p \equiv \frac{2\sigma_c \sin \omega \left[\bar{l}^2 + \cot^2 \omega \right]}{\bar{l}^2 (\bar{l} \cos \omega + \bar{b})^2}. \quad (7.9)$$

Combining Eqs. (7.8) and (7.9), the strength of the pyramidal core can be given in terms of the micro-buckling strength σ_{\max} of the laminate as:

$$\frac{\sigma_p}{\sigma_{\max}} = \frac{2 \sin \omega [\bar{l}^2 + \cot^2 \omega]}{(\bar{l} \cos \omega + \bar{b})^2 \left[\bar{l}^2 + \frac{\cot \omega}{\bar{\phi}} \right]}. \quad (7.10)$$

In the limit of vanishing node volume, the above expression reduces to:

$$\frac{\sigma_p}{\sigma_{\max}} \approx \frac{2 \sin \omega [\bar{l}^2 + \cot^2 \omega]}{\bar{l}^2 \cos^2 \omega \left[\bar{l}^2 + \frac{\cot \omega}{\bar{\phi}} \right]} = \frac{\sin^2 \omega \bar{\rho}}{\left[1 + \frac{\bar{\rho} \cos^3 \omega}{2\bar{\phi}} \right]} \left[1 + \frac{\bar{\rho} \cos^4 \omega}{2} \right]. \quad (7.11)$$

7.2.2 Delamination Failure of the Struts

In this mode we neglect the shear stresses in the struts and consider them as pin-jointed at the ends. An upper bound work calculation [44] then gives the strength of the pyramidal core in terms of the delamination failure stress σ_{dl} of the composite struts as:

$$\frac{\sigma_p}{\sigma_{dl}} = \frac{2 \sin \omega}{(\bar{l} \cos \omega + \bar{b})^2}. \quad (7.12)$$

Here we have neglected the effect of the shear stresses on the delamination failure strength σ_{dl} . In the limit of vanishing node volume, the above expression reduces to:

$$\frac{\sigma_p}{\sigma_{dl}} \approx \frac{2 \sin \omega}{\bar{l}^2 \cos^2 \omega} = \frac{\bar{\rho}}{2} \sin^2 \omega. \quad (7.13)$$

7.2.3 Euler Buckling of the Struts

Under through-thickness compression the pyramidal core may collapse by the elastic buckling of the constituent struts. Recall that the Euler buckling load of an end-clamped strut subjected to an axial load [45] is given by:

$$P_E = \frac{4\pi^2 E_s I}{l^2}, \quad (7.14)$$

and thus the nominal compressive collapse strength of the pyramidal core due to the elastic buckling of the constituent struts is given by:

$$\frac{\sigma_p}{\sigma_{\max}} = \frac{2\pi^2 \bar{E}_s \sin \omega [\bar{l}^2 + \cot^2 \omega]}{3\bar{l}^4 (\bar{l} \cos \omega + \bar{b})^2}, \quad (7.15)$$

where $\bar{E}_s \equiv E_s / \sigma_{\max}$. Note that here we have assumed that the buckling load (7.14) is unaffected by the transverse shear loading of the strut. In the limit of vanishing node volume, the above expression reduces to:

$$\frac{\sigma_p}{\sigma_{\max}} \approx \bar{E}_s \frac{2\pi^2 \sin \omega [\bar{l}^2 + \cot^2 \omega]}{3\bar{l}^4 \cos^2 \omega} = \bar{E}_s \frac{\pi^2 \cos^2 \omega \sin^3 \omega \bar{\rho}^2}{6} \left[1 + \frac{\bar{\rho} \cos^4 \omega}{2} \right] \quad (7.16)$$

7.3 Comparisons and discussion

Predictions for the transverse stiffness using equation (7.4), are shown in Figure 7.3, plotted against experimental data. For the range of relative densities shown, both the data and predictions depend roughly linear upon $\bar{\rho}$. There is a drop off in predicted stiffness for design 2 as relative density increases. This is understood by considering that the shear forces for design 2 are higher due to the decrease in truss length for a given relative density. The compressional stiffness predictions are in general agreement with the data.

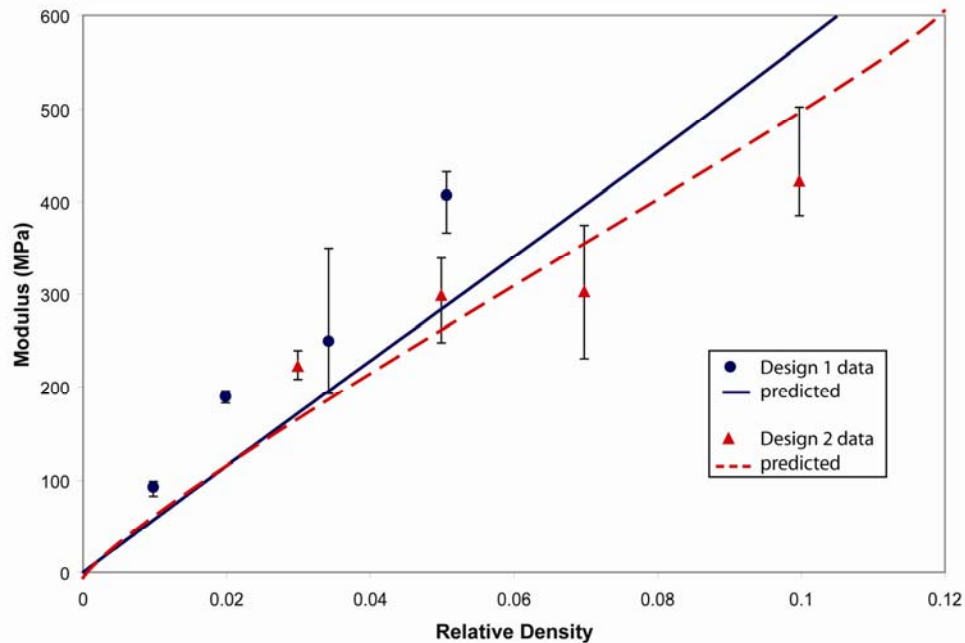


Fig. 7.3 Modulus vs. relative density data plotted with predicted values

Strength predictions are plotted against experiment in Figure 7.4 using equations (7.10) and (7.12). The fiber misalignment ϕ is estimated by using equation (7.6) and literature values for $\tau_y = 70\text{MPa}$ [29], yielding a misalignment $\phi \approx 6.5^\circ$. This value is reasonable considering the potential for alignment errors in the layup and cutting process used to produce the finished trusses. Elastic buckling is active only for very low relative density cores (approx. $\bar{\rho} = 1.5\%$). Above this region, plastic microbuckling and delamination provide upper and lower bounds for the core strength respectively. It was observed in Chapter 6 that clamped truss end conditions produced microbuckling failure and unclamped conditions produced delamination. The end conditions for the trusses in the core lay in between as they were not fully clamped nor can they be considered free ends. It is hypothesized that the end conditions in the truss slightly improve the delamination strength over fully unclamped predictions. As the two mechanisms approach in value, we see a jump in strength for the 10% core in Figure 7.4b.

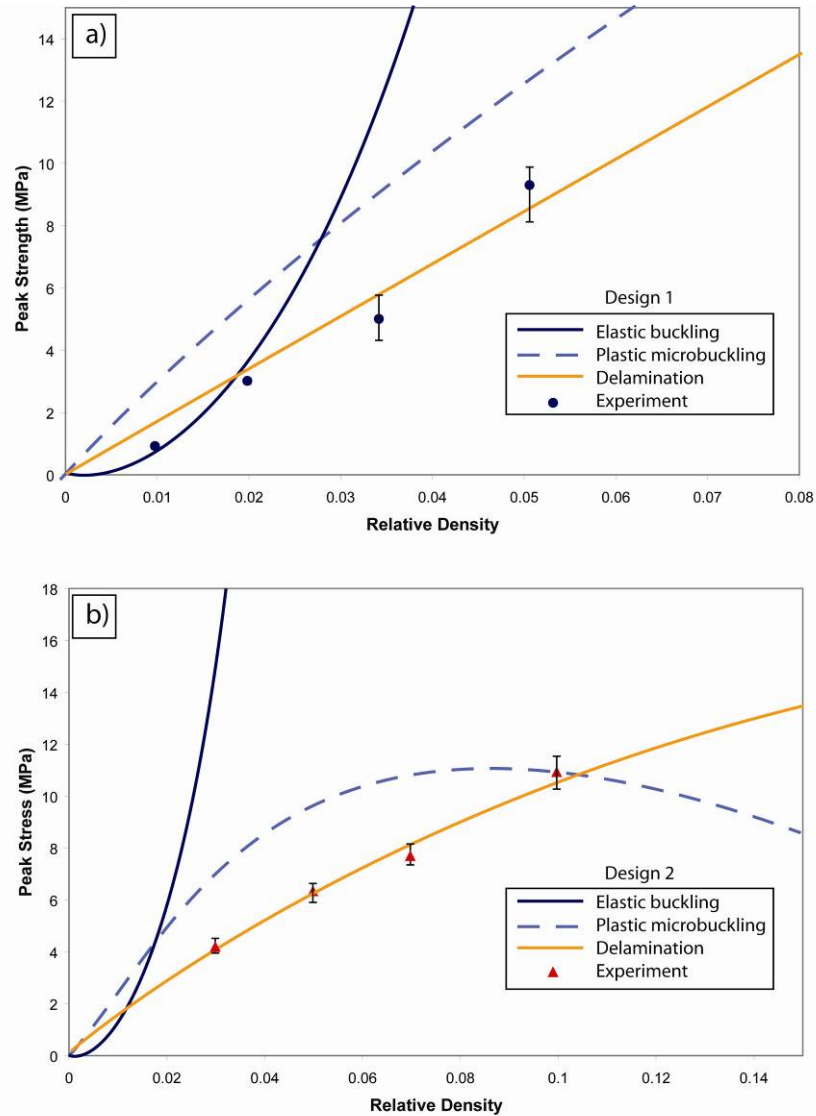


Fig. 7.4 Strength vs. relative density graph with predicted strengths for different failure mechanisms. a) Design 1 and b) Design 2. In order to highlight the regions of interest, the two graphs are plotted on different scales.

It is worth noting here that the analytical model predicts that the peak strength of the design 2 core decreases with increasing relative density for $\bar{\rho} > 8\%$. This is rationalized by noting that with increasing $\bar{\rho}$ an increasing fraction of the composite material is present in the nodes of the pyramidal core and thus not contributing to the overall load carrying capacity. Moreover, the shear stresses in the struts also increase with increasing $\bar{\rho}$. These two factors together, result in the peak strength decreasing with

increasing $\bar{\rho}$ above a critical value of $\bar{\rho}$. Note that since the nodes of the design 1 are about half the size of the nodes of the design 2 cores, the critical density above which σ_p decreases with increasing $\bar{\rho}$ is significantly higher and outside the scale of Figure 7.4a.

It is likely that delamination failure of the struts could be prevented in appropriately designed composite pyramidal cores. In order to illustrate the performance of such an optimized composite pyramidal core, the predicted normalized peak strength, $\sigma_p / (\bar{\rho} \sigma_{\max})$, is plotted in Figure 7.5 as a function of relative density $\bar{\rho}$ only considering the micro-buckling and Euler buckling failure mechanisms of the struts. Predictions are shown for three selected values of \bar{E}_s representative of unidirectional, woven and laminated carbon fiber composites. For the purposes of illustration, we have neglected the volume of the nodes and thus employed equations (7.11) and (7.16) for the micro-buckling and Euler buckling collapse strengths respectively. The expression for relative density found in equation 4.1 reduces in the limit of vanishing node volume ($b = h = c \rightarrow 0$) to:

$$\bar{\rho} = 4\sqrt{2} \left(\frac{t}{l} \right)^2 \quad (7.17)$$

Core parameters are chosen here as $\omega = 45^\circ$ and $\bar{\phi} = 2^\circ$: most experimental evidence [46,49] suggests that the imperfection angle cannot be reduced below 2° in practical biaxial designs while misalignments as low as 0.5° have been reported for specially manufactured unidirectional composites [50]. The normalized strength $\sigma_p / (\bar{\rho} \sigma_{\max})$ is a measure of the efficiency of the topology in terms of its structural strength with $\sigma_p / (\bar{\rho} \sigma_{\max}) \leq 1$: $\sigma_p / (\bar{\rho} \sigma_{\max}) = 1$ corresponding to a cellular material that attains the Voigt upper bound.

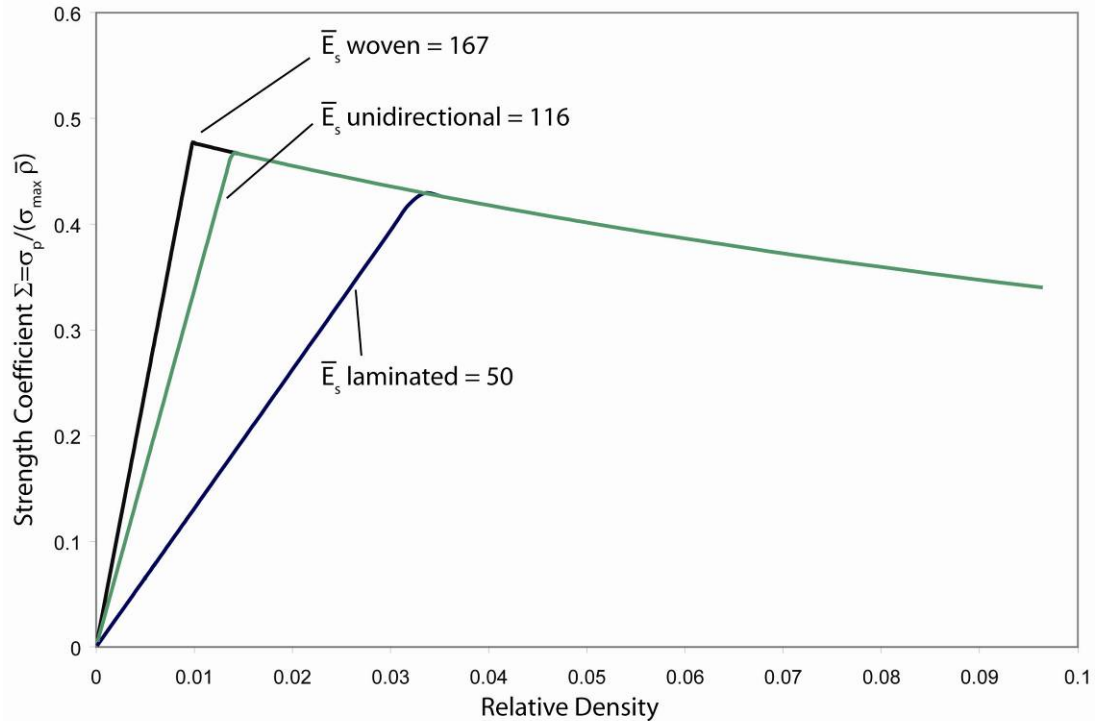


Fig. 7.5 Dimensionless strength coefficient vs. relative density for an ideal pyramidal lattice structure. Dimensionless compressive modulus, $\bar{E}_s = E_s / \sigma_{\max}$, is varied for different fiber arrangements; woven, cross-ply, and unidirectional CFRP composite laminates [50-52]

We note:

- (a) The value of $\bar{\rho}$ at the transition from the Euler buckling to micro-buckling failure modes is most efficient. This is rationalized by noting that in the Euler buckling regime the structural efficiency increases with increasing $\bar{\rho}$ as the struts become more stocky resulting in an increase in their Euler buckling loads. By contrast in the micro-buckling regime with increasing $\bar{\rho}$, the shear forces on the struts increase resulting in a decrease in their micro-buckling stress as per Eq. (7.11).

- (b) The maximum value of $\sigma_p / (\bar{\rho} \sigma_{\max})$ for the pyramidal cores increases with increasing \bar{E}_s with the transition from Euler buckling failure to micro-buckling then occurring at lower values of $\bar{\rho}$.

Chapter 8

Discussion

Several methods for constructing pyramidal lattice core sandwich panels from CFRP materials have been investigated. A bi-axial laminate based, snap-fit truss method was found to fulfill the node constraint requirement. The simple implementation of this manufacturing technique appears scalable with little modification and could be extended to other material systems.

Micromechanical analysis provides understanding of the role of core failure mechanisms and allows upper-bound stiffness and strength predictions to be drawn for pyramidal CFRP lattice sandwich panels. Governing equations regarding the effect of node width on panel performance have been drafted and are in generally good agreement with experiment.. Comparison of the strength performance of CFRP lattice structures to available cellular metal systems is shown in Figure 8.1. The strength to weight ratio for these structures lies in a previously unoccupied region of material space. Even so, the theoretical limit for strength for pyramidal CFRP structures shown as the dashed line in Fig 1.2(a) has not been approached for high relative density cores because of nodal inefficiencies and the activation of delamination modes of failure. It is also noted that the pultruded rod core data from Chapter 2 is competitive with the bi-axial laminate designs. The structural efficiency of the pultruded rod design was limited by its node push-out failure mechanism. This offset the high strength of the unidirectional composite resulting in comparable peak strengths.

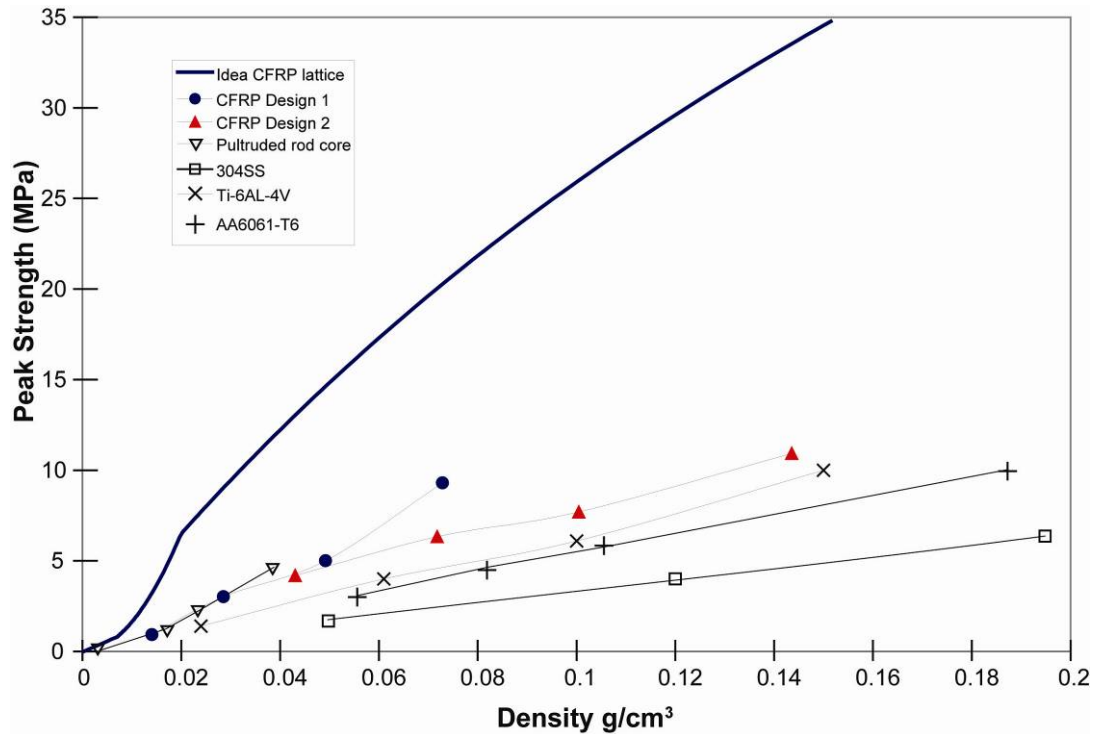


Fig. 8.1 Comparison of experimental pyramidal lattice strength vs. density. The predicted strength for an ideal CFRP lattice is plotted as an upper bound on core strength.

The compressive moduli of pyramidal CFRP lattice cores were found to be low. Even in the ideal limiting case of negligible node volume, the predicted stiffness would not fill a gap in stiff-lightweight materials due to the $\bar{\rho} \cdot \sin^4(\omega)$ term in equation (7.5). Only as $\omega \rightarrow 90^\circ$ would the sandwich panel stiffness approach the gap region in Fig. 1.2b.

There are many geometric factors to take into account when considering a fibrous composite lattice structure like the ones presented here. The entire cell geometry combined with the size and shape of the cross section and the layout of the fiber all greatly influence the final properties of the cellular material. If the weaker types of failure modes, such as delamination, can be suppressed by changing the geometry of the system, then there exists the potential for CFRP lattice structures to push closer to the theoretical

boundaries for lightweight/strong cellular material and further fill in the vacancy in material space.

Chapter 9

Conclusions

- Lattices made from CFRP composites with fibers oriented in the principle load direction are anticipated to exceed the specific strength of other cellular materials.
- We have investigated three approaches for the fabrication of CFRP composite sandwich panels with pyramidal lattice cores in the relative density range 0.1-10%.
- An approach using pultruded rods with all the fibers in the truss aligned in the axial direction, utilized adhesive bonding of trusses to pre-drilled facesheets. Failure transitioned to a node shear mode as $\bar{\rho}$ increased and this approach was therefore inefficient for higher relative densities.
- A method for constructing pyramidal cores from unidirectional laminates utilizing milled facesheet slots was developed. The node shear failure mode was observed and it resulted in premature failure. This method also proved inefficient at higher relative densities.
- Bi-axial laminates were used in a third approach utilizing a snap-fit construction method and milled facesheet slots for the nodes. This method successfully prevented node failure and two different core designs were created using this method. The compressive modulus of Design 1 ranged 92-407MPa and the compressive strength ranged over 0.9 - 9.3MPa for relative densities 1,2,3.5 and 5%. The compressive modulus of Design 2 ranged from 222-422MPa with a compressive strength range of 4-11MPa for relative densities 3,5,7 and 10%

- Micromechanical models were developed describing the failure mechanisms observed in the panels. The predictions agree well with the experimental data and give indications as to the obtainable peak strength for pyramidal CFRP lattice core structures as well as reveal the most weight-efficient designs and relative densities.
- If delamination modes of failure can be inhibited, the analysis indicates that pyramidal CFRP lattice cores have the potential to be among the highest strength/weight cellular materials developed to date and would occupy the gap identified by Ashby in material strength-relative density space.

References

- [1] J.M.Davies, *Lightweight Sandwich Construction*. Blackwell Publishing Inc. (2001)
- [2] Joseph F. Hanlon, et. al, "Handbook of Package Engineering, 3rd Edition" CRC Press LLC (1998)
- [3] S. P. Timoshenko, S.Woinowsky- Kreiger "Theory of Plates and Shells" McGraw-Hill Publishing Co. (1964)
- [4] V.L.Tagarielli, N.A.Fleck, V.S.Deshpande, Collapse of clamped and simply supported composite sandwich beams in three-point bending. *Composites: Part B* 35 (2004) 523-534
- [5] Suh, Kyung W. et. al., "Lightweight Cellular Plastics" *Advanced Materials* (2000), 12, No. 23 Wiley publishing.
- [6] T. J. Lu, H. A. Stone and M. F. Ashby, "Heat Transfer in Open-Cell Metal Foams, *Acta Materialia*, Vol. 46 Iss. 10 (1998) pp. 3619-3635
- [7] T. Wen, J. Tian, T. J. Lu, D. T. Queheillalt, H. N. G. Wadley, Forced Convection in Metallic Honeycomb Structures, *International Journal of Heat and Mass Transfer* 49 (2006) 3313-3324
- [8] Craig A. Steeves, Norman A. Fleck, Material selection in sandwich beam construction. *Scripta Materialia* 50 (2004) 1335-1339
- [9] Deshpande, V.S., Ashby, M.F., Fleck, N.A., 2001a. Foam topology: bending versus stretching dominated architectures. *Acta Materialia* 49, 1035
- [10] M.F. Ashby, et al., "Metal Foams: A Design Guide" Butterworth-Heinemann, Woburn, MA, 2000
- [11] M. Ashby, D.R.H. Jones, "Engineering Materials 2, 3rd Edition: An Introduction to Microstructures, Processing and Design" Butterworth-Heinemann (2005)
- [12] L.J. Gibson, M.F. Ashby, "Cellular Solids, Structure and Properties" 2nd Edition, Cambridge, Cambridge University Press (1997)
- [13] M.F. Ashby, *Materials Selection in Mechanical Design*. , Pergamon Press, New York (1992)
- [14] N. Waterman, Mike Ashby, "The materials Selector, Second Edition" Chapman & Hall/CRC (1996)

- [15] M. F. Ashby, Granta Design CES EduPack, Cambridge (2004)
<http://www.grantadesign.com>
- [16] Lee, James L., Zeng, Changchun et. al., “Polymer nanocomposite foams”
Composites Science and Technology (2005) Elsevier
- [17] Banhart, John, “Manufacture, characterization and application of cellular metals and metal foams” Progress in Materials Science 46 (2001) Elsevier Press
- [18] L. Montnaro, et. al., “Ceramic Foams by Powder Processing” Journal of the European Ceramic Society (1998) Elsevier Science Ltd.
- [19] Woesz, Alexander et. al., “Cellular Solids; beyond the Apparent Density-an Experimental Assessment of Mechanical Properties” Advanced Engineering Materials (2004) Wiley publishing
- [20] V. Sendjarevic, D. Klempner, "Polymeric Foams and Foam Technology" Hanser Gardner Publications; 2nd edition (April 2004)
- [21] T. Ide, M. Tane et. al., “Compressive properties of lotus-type porous stainless steel” (2006) J. Mater. Res., Vol.21, No. 1 Materials Research Society
- [22] Bitzer T. 1997. Honeycomb Technology: Materials, Design, Manufacturing, Applications and Testing. Chapman & Hall USA, 115 Fifth Avenue, New York, NY 10003, USA
- [23] M.F. Ashby. The properties of foams and lattices. Philosophical Transactions of the Royal Society A, In Press
- [24] Douglas T. Queheillalt, David J. Sypeck, Haydn N.G. Wadley, “Ultrasonic characterization of cellular metal structures” (2002) Materials Science and Engineering A323 pp.138-147 Elsevier
- [25] S. Nemat-Nasser, W. J. Kang, J. D. McGee, W.-G. Guo, J. B. Isaacs, Experimental Investigation of Energy-Absorption Characteristics of Components of Sandwich Structures, International Journal of Impace Engineering 34 (2006) 1119-1146
- [26] Kooistra, G.W. Lattice truss structures made from age hardenable aluminum alloys. Masters Thesis, Department of Materials Science and Engineering. University of Virginia, 2005
- [27] M. F. Ashby, Y.J.M. Bréchet, “Designing hybrid materials” Acta Materialia 51 (2003) 5801-5821 Elsevier Ltd.

- [28] Zhenyu Xue, John W. Hutchinson, "Constitutive Model for Quasi-Static Deformation of Metallic Sandwich Cores" International Journal for Numerical Methods in Engineering, John Wiley & Sons 2004
- [29] Engineered Materials Handbook, ASM International USA (1987)
- [30] A.G. Evans, et. al., "The topological design of multifunctional cellular metals" (2001) Progress in Materials Science 46 pp. 309-327 Elsevier
- [31] Wadley, H.N.G., Fleck, N.A., Evans, A.G., 2003. Fabrication and structural performance of periodic cellular metal sandwich structures. Composite Science and Technology 63 (16), 2331-2343
- [32] N.A. Fleck. Compressive Failure of Fiber Composites. Advances in Applied Mechanics, Vol 33. Cambridge University Academic Press (1997)
- [33] Queheillalt, D.T., Wadley, H.N.G. Pyramidal lattice truss structures with hollow trusses. Materials Science and Engineering A 397 (2005) pg.132
- [34] Kooistra, G.W., Waley, H.N.G., 2005. Lattice truss structures from expanded metal sheets. Materials and Design, In Press.
- [35] Hemen Ray, "Investigation of advanced lightweight sandwich structural concept" Naval Air Warfare Center, Aircraft Division, Code 433100R08, Warminster, PA (1993)
- [36] Andrea I. Marasco, Denis D.R. Cartié, Ivana K. Partridge, Amir Rezai, "Mechanical properties balance in novel Z-pinned sandwich panels: Out-of-plane properties," Composites: Part Axx (2005) 1-8
- [37] M. K. Bannister, R. Braemar, P. J. Crothers, "The mechanical performance of 3D woven sandwich composites" Composite Structures 47 (1999) 687-690 Elsevier Science Ltd.
- [38] Douglas T. Queheillalt, Haydn N.G. Wadley, "Fabrication and Mechanical Properties of Pyramidal Lattice Truss Structures with Perfect nodes" In-Prep (submitted to Scripta Materialia February 2007)
- [39] Fibreglast 2000/2006 material data sheet (website) <http://www.fibreglast.com>
- [40] Vikram Deshpande, private communication, 2007
- [41] Herakovich, Carl T. Mechanics of Fibrous Composites. John Wiley & Sons, Inc. 605 Third Avenue, New York, NY (1998)
- [42] Donald Adams, "Testing cross-ply vs. Unidirectional composites" High Performance Composites, March 2006 Ray Publishing

- [43] Donald Adams, "Current compression test methods" High Performance Composites, May 2005 Ray Publishing
- [44] K. Finnegan, et. al., "The compressive response of carbon fiber composite pyramidal truss sandwich cores" (2007 in-prep)
- [45] R.C. Hbbeler, "Mechanics of Materials 5th Edition" Pearson Education, Inc. , New Jersey (2003)
- [46] Aboudi, Jacob, "Mechanics of Composite Materials, A Unified Micromechanical Approach" Elsevier Science Publishing Company, Inc. 655 Avenue of the Americas, New York, NY 1991
- [47] Argon, A. S., "Fracture of composites" Treatise of Material Science and Technology. (1972) vol 1, pp. 79-114 Academic Press, New York, NY
- [48] B. Budiansky, N.A. Fleck, "Compressive failure of fibre composites" J. Mech. Phys. Solids, vol. 41, no. 1, pp. 183-211 (1993)
- [49] Yurgatis, S. W. "Measurement of small angle misalignments in continuous fibre composites" Composites Science and Technology (1987) 30, 279-293
- [50] Graphlite material data sheet (website) <http://www.aviasport.net>
- [51] N.A. Fleck, P.M. Jelf, P.T. Curtis, "Compressive Failure of Laminated and Woven Composites" J. Composites Technology & Research, Vol. 17, no. 3, (1995)
- [52] Chung, D.D.L, "Carbon Fiber Composites" Elsevier (1994)
- [53] I.W. Hall, M. Guden, T.D. Claar, "Transverse and longitudinal crushing of aluminum-foam filled tubes" Scripta Materialia 46 (2002) 513-518 Elsevier Science Ltd.
- [54] John Currey, "The Mechanical Adaptation of Bones" (1984) Princeton University Press, Princeton NJ
- [55] Matt Wedel (photographer) on display at the Natural History Museum, London (2006)
- [56] V.S. Deshpande, N.A. Fleck, M.F. Ashby, "Effective properties of the octet-truss lattice material" J. Mech and Phys. Sol. 49 (2001) 1747-1769 Elsevier Science Ltd.

Appendix A Unidirectional Laminate $\bar{\rho}$ Calculation

Figure A.1 shows the unit cell for a pyramidal unidirectional laminate core. The height of the unit cell is: $l \sin \omega$.

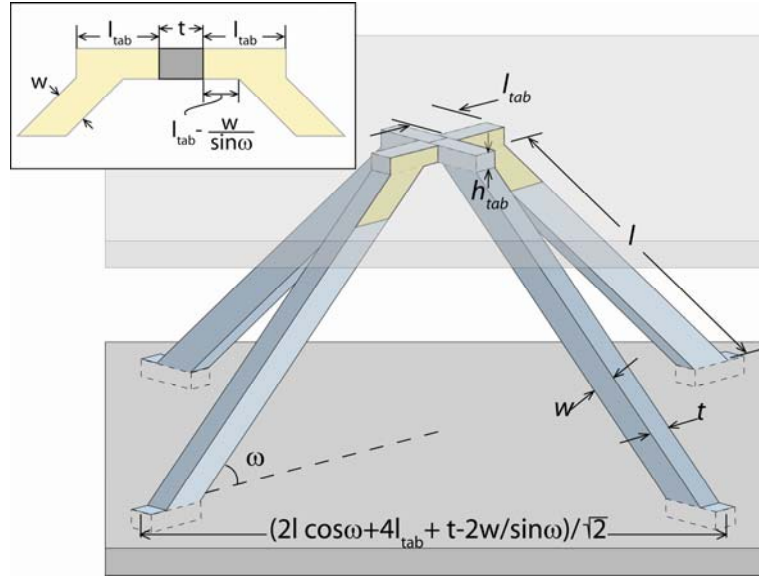


Fig. A.1 Unidirectional Laminate Core Unit Cell Geometry

Since the tabs are completely buried in the facesheet, they are considered part of the facesheet and their mass contribution to the core is ignored. The volume of the unit cell follows as:

$$V_{cell} = \frac{1}{2} \left(2l \cos \omega + 4l_{tab} + t - \frac{2w}{\sin \omega} \right)^2 l \sin \omega \quad (\text{A.1})$$

The volume of the truss members occupying the unit cell is written simply:

$$V_{core} = 4ltw \quad (\text{A.2})$$

The relative density for the core is then written as:

$$\bar{\rho} = \frac{4ltw}{\frac{1}{2} l \sin \omega \left(2l \cos \omega + 4l_{tab} + t - \frac{2w}{\sin \omega} \right)^2} = \frac{2tw}{\left(l \cos \omega + 2l_{tab} + \frac{1}{2}t - \frac{w}{\sin \omega} \right)^2 \sin \omega} \quad (\text{A.3})$$

Appendix B

Bi-directional Laminate $\bar{\rho}$ Calculation

Figure B.1 shows the bi-directional laminate unit cell geometry. The square defining the base of the unit cell has corners placed in the center of the nodes.

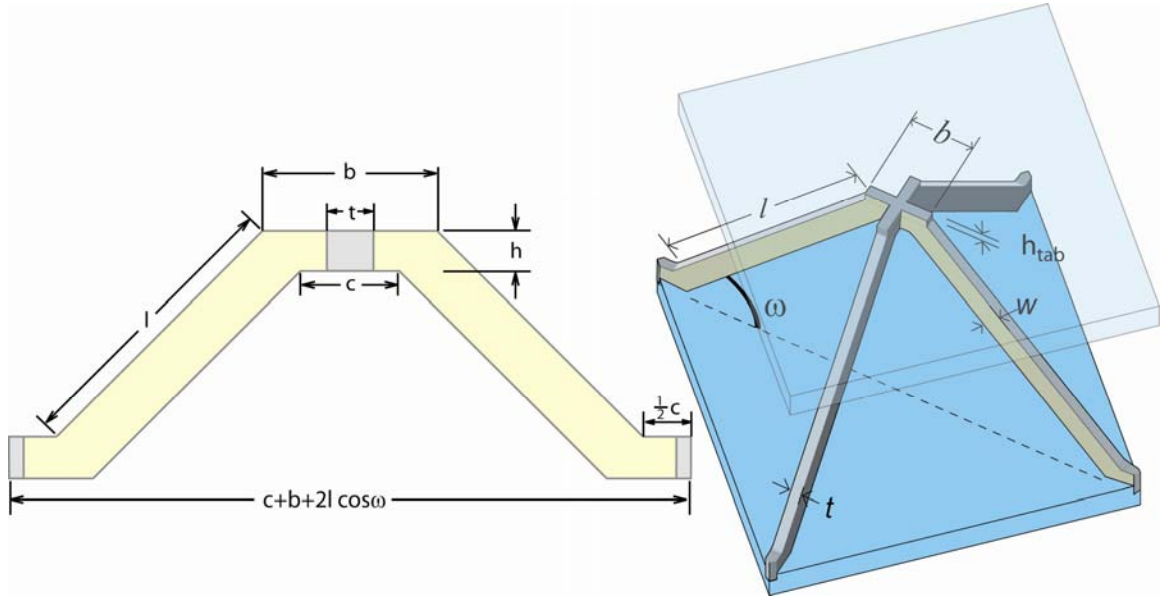


Fig. B.1 bi-directional unit cell geometry planar and isometric view.

The volume of the unit cell is given by:

$$V_{cell} = (l \sin \omega + h) \frac{1}{2} (2l \cos \omega + b + c)^2 \quad (\text{B.1})$$

The center of the node is material shared by the two intersecting cut-out patterns (darker shaded areas in the planar view) and has a volume of $t^2 h$. Each unit cell has two nodes, with one full node in the center and a quarter node at each corner of the base. The volume of the core follows as:

$$V_{core} = 2(th(c-t) + 2ltw + bht) \quad (\text{B.2})$$

The relative density for the core can now be written:

$$\bar{\rho} = \frac{2(th(c-t) + 2ltw + bht)}{(l \sin \omega + h) \frac{1}{2} (2l \cos \omega + b + c)^2} = \frac{2(ltw + \frac{1}{2} ht(b+c-t))}{(l \sin \omega + h)(l \cos \omega + \frac{1}{2} (b+c))^2} \quad (\text{B.3})$$